ELSEVIER

Metal–organic frameworks: Structures and functional applications

Long Jiao [1], Joanne Yen Ru Seow [2], William Scott Skinner [2], Zhiyong U. Wang [2,*], Hai-Long Jiang [1,*]

[1] Hefei National Laboratory for Physical Sciences at the Microscale, Collaborative Innovation Center of Suzhou Nano Science and Technology Department of Chemistry, University of Science and Technology of China, Hefei, Anhui 230026, PR China
[2] Department of Chemistry and Physics, Troy University, Troy, AL 36082, United States

Metal–organic frameworks (MOFs), constructed by organic linkers and metal nodes, are a new class of crystalline porous materials with significant application potentials. Featured with extremely high surface area, large porosity, tunable pore size, and flexible functionality, MOFs have gained extensive explorations as a highly versatile platform for functional applications in many research fields. This review presents an up-to-date summary ranging from the structural and physical properties of MOFs to their recent application advances including gas storage and separation, heterogeneous catalysis, chemical sensors, proton conductivity, biomedicine, and others. The structure–property relationships are particularly emphasized. Finally, the newly emerging research trends of MOFs and the unresolved challenges for functional applications are discussed in detail.

Dedicated to Professor Jin-Shun Huang on the occasion of his 80th birthday.

Introduction

In the past three decades, porous materials have attracted great attention in many fields of exploration including physics, chemistry, and material science [1–4]. With wide applications in areas such as adsorption, separation, biomedicine, as well as catalysis, porous materials are playing significant roles in our daily activities. Classical porous materials like activated carbons and zeolites have been found in wide practical applications with their low cost and superior stability but still suffer from problems such as non-uniform structure, irregular pores, and lack of clear structure–property relationships. Consequently, the exploration of better performing advanced porous materials for these applications continues to be an intense area of scientific research.

Metal–organic frameworks (MOFs), also known as porous coordination polymers (PCPs), are constructed by organic linkers and metal ions or clusters and have emerged as a new type of crystalline materials with large surface area (typically ranging from 1000 to 10,000 m^2/g), high porosity, tunable structures, and flexible tailorability, compared with traditional porous materials such as zeolites and activated carbons [5–7]. The field of MOFs has been well developed in the past two decades and is still fast growing, with thousands of papers published each year (Fig. 1). Featuring diversified structures and highly tunable pore sizes (usually 0–3 nm, up to 9.8 nm), MOFs are able to cover the full pore size gap between microporous zeolites and mesoporous silicas. With a large variety of metal nodes and theoretically unlimited number of organic linkers, one can easily tune the compositions and structures of MOFs to achieve targeted functionality in a precise manner. MOFs have been extensively studied for a diverse range of applications including gas sorption and separation, chemical sensors, biomedicine, proton conductivity, heterogeneous catalysis, and others [5–11]. In addition, the well-defined and tailorable crystalline structures of MOFs make them an ideal platform for the establishment of clear structure–property relationships, which is of great significance for

* Corresponding authors.
E-mail addresses: Wang, Z.U. (wangz@troy.edu), Jiang, H.-L. (jianglab@ustc.edu.cn).

 https://doi.org/10.1016/j.mattod.2018.10.038

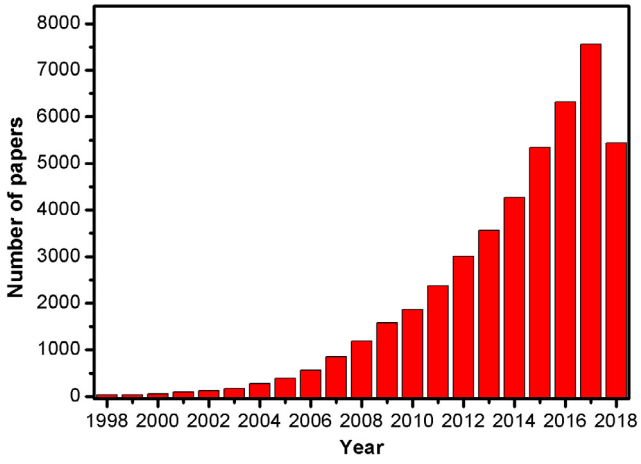

FIGURE 1

The number of MOF-related research papers published each year from 1998 to 2018. ISI web of knowledge data by searching key words of "metal–organic framework" or "porous coordination polymer" on August 15, 2018.

phenomenological understanding and thus provides guides for the design of new functional materials [12].

In this review, we first discuss the unique structural advantages of MOFs and their physical properties, including stability, pore characters, and surface area, for practical applications. We then provide a systematic summary on the exploration of MOFs in various functional applications while emphasizing the structure–property relationships. Next, we would like to summarize the newly developed trends and areas of MOFs emerging in recent years. Finally, the prospect on the unresolved challenges of MOFs will be presented. Considering that many MOF-related reviews have been published in recent years, we would like to mainly focus on the most recent and newly developed functional applications while directing the readers to other existing reviews of specific fields where appropriate.

Structures of MOFs

The diverse crystalline structures of MOFs provide the basis for their multiple functions. MOFs are constructed by joining metals or metal clusters (also called secondary building units, SBUs) with organic linkers which are mostly carboxylic acid or nitrogen-containing ligands (Figs. 2 and 3) [13–16]. Some representative SBUs and organic linkers are illustrated in Fig. 2. One unique feature of MOFs compared to other porous materials such as zeolites and carbons is the tunability. As the structures of MOFs are determined by the geometry of SBUs as well as the shape and size of the organic ligands, MOFs can be tuned in a certain degree as expected by judiciously selecting SBUs and linkers to have the desired pore size, structure, and functionality for specific applications. As a representative example, Yaghi et al. demonstrated that an isoreticular series of MOF-74 structures (IRMOF-74-n) can be generated by systematically elongating the ligand structure [17]. While the microporous IRMOF-74-I can accommodate small gas molecules such as N_2 and CO_2, the much larger macroporous IRMOF-74-VII and IRMOF-74-IX can hold proteins such as the green fluorescent protein. In theory, the MOF structures can be predicted based on the metals and the organic linker building blocks. Recently, it was estimated that over 20,000 MOF structures had been reported [7], and the number is still increasing by thousands each year. The defined structures of MOFs make it possible to study the structure–property relationships, which is critical for the rational design of new MOFs with desired functional applications.

The functional sites of MOF materials can be generated from the pore surfaces (Fig. 3). For example, functional groups such as pyridyl and amine that are capable of recognizing specific small molecules can be directly incorporated into the organic linkers. The recently developed multivariate MOFs can readily introduce multiple functional sites onto the pore surfaces. Post-synthetic modification of the SBUs or organic linkers can introduce functional groups which are incompatible with MOF synthesis. The metal ions/clusters and organic ligands of MOFs bearing different electronic, magnetic, and optical properties can be carefully tuned to match the specific application. In addition, the pore space in MOFs can be furnished with diverse functional guests for multiple functions. MOFs have pore sizes ranging from microporous to macroporous and can accommodate diverse species such as single metal atoms, nanoparticles, metal complexes, organic dyes, polyoxometalates, polymers, and small enzymes [13–18]. The guest species can significantly extend the applications that cannot be achieved with single MOFs.

Physical properties of MOFs

Stability

Although a great number of new structures have been reported over the past two decades, MOFs usually suffer from weak stability, such as poor water stability, acid/base stability, thermal stability, and mechanical stability. Nevertheless, the stability of MOFs is essential for various practical applications. To address this challenge, much endeavor has been made and significant progress has been achieved in recent years [19–22].

The degradation of MOFs in water vapor or liquid water can be observed as a series of substitution reactions in which the metal-coordinated linkers are replaced by water or hydroxide. Thus, the direct method to improve the stability of MOFs is to increase the strength of the coordination bonds between SBUs and organic linkers. Up to now, some water-stable MOFs that have been extensively studied include the chromium-based MIL-101 series [23], zeolitic imidazolate frameworks (ZIFs) [24] or metal azolate frameworks (MAFs) [25], the zirconium-based carboxylates [26–32], the aluminum-based carboxylates [33], the pyrazole-based MOFs [34] and others. Additionally, new strategies by specially creating hydrophobic surfaces or interfaces to improve the water/moisture stability of MOFs have also been developed recently. Nguyen and Cohen developed an efficient strategy by the integration of medium to long alkyl groups within IRMOF-3, which could shield the moisture-sensitive MOF by turning it into a hydrophobic material [35]. Yang et al. reported a series of fluorinated MOFs (FMOFs) with remarkable water stability as a result of super-hydrophobicity [36]. Jiang and coworkers synthesized a novel and highly stable MOF (USTC-6) with a corrugated $-CF_3$ surface that features high hydrophobicity [37]. Yang and Park improved the water stability of IRMOF-1 by converting the organic ligands on the MOF surface into an amorphous carbon layer via heating under nitrogen

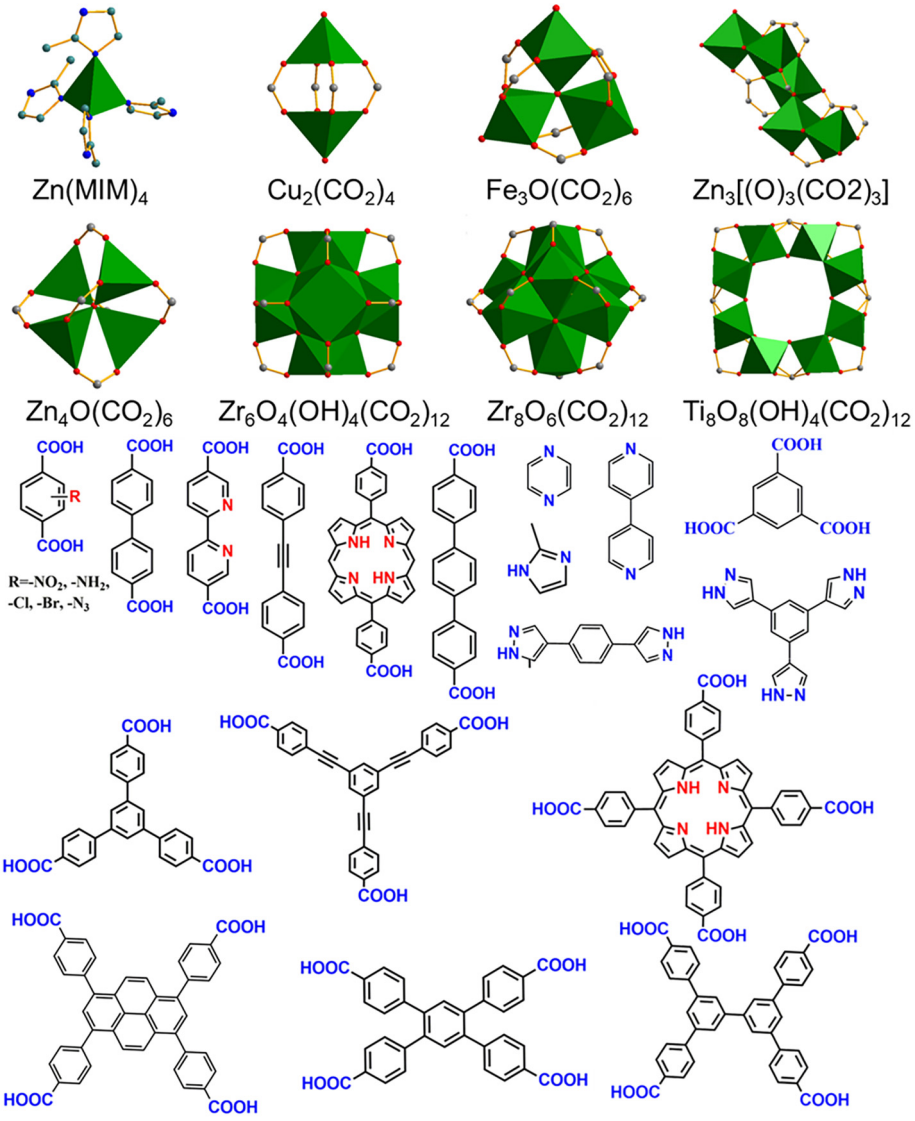

FIGURE 2

Some representative SBUs and organic linkers for MOFs.

while maintaining the structure and pore size distribution [38]. Zhang et al. greatly improved the moisture/water stability of water-labile MOFs by decorating their surface with hydrophobic and permeable polydimethylsiloxane (PDMS) thin layers via vapor deposition technique. The surface modification almost does not change the surface area of the original MOFs (Fig. 4a) [39]. By incorporating MOFs into polymers, Shih et al. developed MOF-polymer composites that show enhanced water stability in reference to the pristine MOF [40]. Singh et al. grafted cholesterol (CHS) to the surface of γ-cyclodextrin based MOFs (CD-MOFs) to form a protective hydrophobic layer in order to improve their aqueous stability. As a result, the CHS shielded CD-MOFs prove to be hydrophobic with a significant enhancement in water stability and maintain the crystalline structure [41]. Ma and coworkers treated Zr-based UiO-66, UiO-66-SO_3H, and PCN-222 with *n*-octadecylphosphonic acid (OPA) and yielded superhydrophobic materials with contact angles greater than 150°. The long alkyl chains positioned on the MOF's surface would not block the inherent porosity of the frameworks, but generate high water resistance and keep them stable under various aqueous conditions. The materials were able to separate the organic solvent chloroform from a mixture with water [42]. In addition to the decoration of outside surface, Ding et al. modified the inside channels of MOF-5 via *in situ* polymerization of aromatic acetylenes. The thus-obtained MOF material can capture and trap CO_2 molecules and effectively retards the diffusion and repels water molecules (Fig. 4b) [43]. Furthermore, many other approaches that can alter the thermodynamic stability factors of the framework have also been reported. Zhu et al. found that doping metal ions (Cu^{2+}, Cd^{2+}, or Fe^{2+}) into a gyroidal MOF, STU-1A, resulting in heterometallic MOFs with exceptional water stability [44]. Feng et al. inserted the additional chelating bipyridine moiety in the ligand 5,5′-((thiophene-2,5-dicarbonyl)bis(azane diyl))diisophthalic acid and turned the interpenetrated framework NKU-112 ($[Ni_2L1(\mu_2\text{-}H_2O)(H_2O)_2(DMF)_2]\cdot(solvents)_n$) into the self-penetrated framework NKU-113 ($[Co_2L2(\mu_2\text{-}H_2O)(H_2O)_2]\cdot(solvents)_n$). The change in structure topology resulted in enhanced porosity and stability [45]. Bae et al. treated

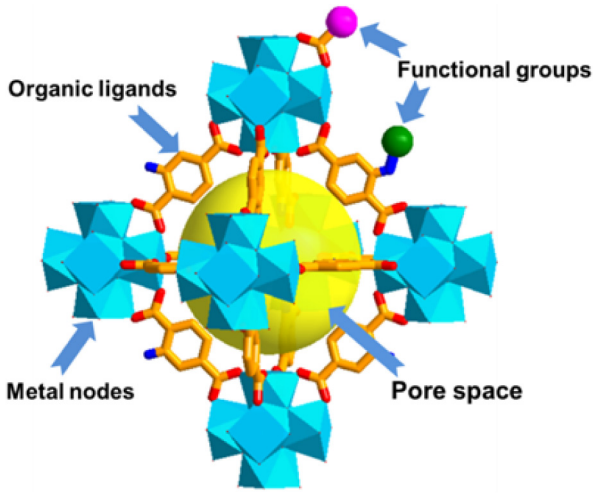

FIGURE 3

Illustration for the construction elements of functional MOFs.

HKUST-1 with O_2 plasma and retained the MOF's porosity after hours of exposure to moisture [46]. This method works by increasing the surface polarity of the MOF.

Compared to water/moisture stability, it is more challenging to construct stable MOFs with good acid/base stability. According to the hard/soft acid/base (HSAB) principle, the interactions between hard Lewis acids and bases, or soft Lewis acids and bases are much stronger than those between hard acids and soft bases, or soft acids and hard bases [47]. There has been significant progress of developing MOFs with stabilities under strongly acidic, basic, or other harsh conditions. A common design strategy is to combine the high oxidation-state metal ions (hard acids) with the carboxylate ligands (hard bases) to generate strong bonds which are resistant toward chemical attack. Among them, Zr-based MOFs are particularly noteworthy due to their rich structure types, excellent stability, and diverse properties and functions [28,48]. For example, Feng et al. employed Fe-TCPP (TCPP = tetrakis(4carboxyphenyl)porphyrin) as a heme-like ligand and Zr_6 clusters as nodes to afford a highly stable,

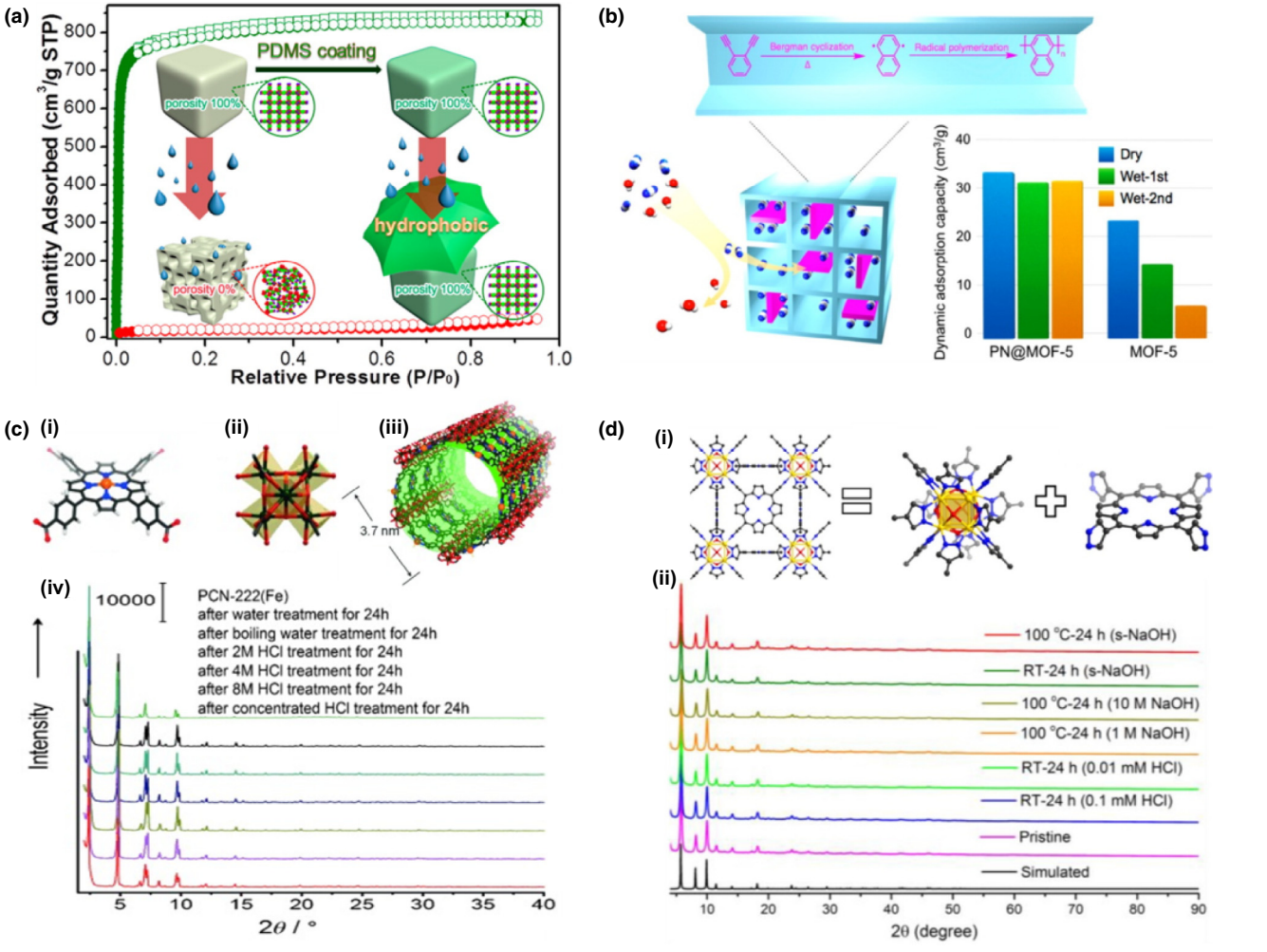

FIGURE 4

(a) Illustration of PDMS-coating on the MOF surface for improving the moisture/water resistance [39]. Reproduced with permission from Ref. [39]. Copyright 2014, American Chemical Society. (b) Illustration of competitive adsorption of CO_2 against H_2O at PN@MOF-5 [43]. Reproduced with permission from Ref. [43]. Copyright 2016, American Chemical Society. (c) Crystal structure and stability test of PCN-222(Fe) [28]. Adapted with permission from Ref. [28]. Copyright 2012, Wiley-VCH. (d) Crystal structure and stability test of PCN-601 [56]. Adapted with permission from Ref. [56]. Copyright 2016, American Chemical Society.

mesoporous MOF, PCN-222(Fe), which can remain stable in 8 M HCl for 24 h (Fig. 4c) [28]. Other metals like lanthanides, cobalt, nickel, manganese, and cadmium are also good for constructing stable MOFs. Duan et al. developed La^{3+}-containing [La(BTB)H_2O]·solvent (H_3BTB = 1,3,5-tris(4-carboxyphenyl)benzene) which remained stable in aqueous solutions of pH 2 to 14 at 100 °C for three days [49]. After that, they further developed another La^{3+}-containing MOF, [La(BTN)DMF]·guest (H_3BTN = 1,3,5-tri(6-hydroxycarbonylnaphthalen-2-yl)benzene), which was stable in 100 °C aqueous HCl (pH = 2) and NaOH (pH = 12) solutions [50]. Gong et al. developed [La(TTCA)(H_2O)]·DMF·H_2O ($TTCA^{3-}$ = triphenylene-2,6,10-tricarboxylate) which was stable in aqueous solutions of pH 1 to 13 for seven days [51]. Dong et al. synthesized three lanthanide zeolites [$Ln_3(\mu_6\text{-}CO_3)(\mu_3\text{-}OH)_6$]OH (Ln = Gd, Tb, and Dy) as catalysts for the cycloaddition reactions of CO_2 with epoxides to form cyclic carbonates [52]. These MOFs cannot survive strongly acidic conditions (1 M HCl) but are otherwise stable in dilute acid (0.1 M HCl) for hours and in extremely basic conditions (20 M NaOH) for days. Lu et al. constructed Co^{2+}-containing MAFX27-OH ([$Co_2(\mu\text{-}OH)_2$(bbta)], H_2bbta = 1*H*,5*H*-benzo(1,2-*d*:4,5-*d*′)bistriazole) which was stable in 1.0 M KOH solution [53]. Yang et al. constructed [$Co_2(OH)_2C_8H_4O_4$] ($C_8H_4O_4$ = terephthalate) as a supercapacitor electrode, presenting ultrahigh stability in 5 M KOH under electrochemical conditions [54]. Yi et al. synthesized Cd^{2+}-based [Cd_3(L)$(bipy)_2$·4DMA]$_n$ as an effective luminescent sensor and adsorbent material for benzene vapor [55]. The MOF was stable in aqueous solutions of pH 2–13 at room temperature for 24 h. Wang et al. developed a Ni^{2+}-containing pyrazolate-based porphyrinic PCN-601 which showed extraordinary base resistance in saturated NaOH (20 M) at 100 °C for 24 h (Fig. 4d) [56]. This is the first example of MOFs that can retain its crystallinity and porosity in saturated NaOH solution (~20 mol/L) at room temperature and 100 °C. By elongating the porphyrinic pyrazolate ligand in PCN-601, Lv et al. also constructed the isoreticular PCN-602(M) (M = Ni and Mn) as catalysts and the MOFs were stable in aqueous solutions of pH 4–14 at room temperature for 24 h [57]. Colombo et al. reported a pyrazolate-bridged MOF of the type $Ni_3(BTP)_2$·xsolvent (H_3BTP = 1,3,5-tris(1H-pyrazol-4-yl)benzene), presenting ultrahigh stability to the treatment of boiling solutions with pH from 2 to 14 for two weeks [34].

The thermal stability of MOFs is also important for applications requiring elevated temperatures, such as high-temperature gas phase reactions. Thermal stability is generally determined by the node-linker bond strength and the number of linkers connected to each metal node. High valence metal ions such as Ln^{3+}, Al^{3+}, Zr^{4+}, and Ti^{4+} often generate MOFs with high thermal stability. While most MOFs are stable up to 350–400 °C, selected ones such as MIL-53 [33] and UiO-66 [26] are stable above 500 °C. In addition to the mostly used MOFs with high thermal stability such as MIL-53 and UiO-66, Ibarra et al. synthesized a Sc(III)-based MOFs (NOTT-400) based on the [$Sc_2(\mu_2\text{-}OH)(O_2CR)_4$] building block, showing an excellent thermal stability up to 520 °C [58]. Banerjee et al. reported two lithium-based metal–organic frameworks, $Li_2(C_{14}H_8O_4)$[Li_2(4,4′-BPDC) and $Li_2(C_{14}H_8O_6S)$ [Li_2(4,4′-SDB), both of which are stable up to 575 and 500 °C, respectively [59]. By switching the ligand to 2,6-napthalenedicarboxylate (2,6-NDC), the researchers also prepared Li_2(2,6-NDC) that was stable up to 610 °C [60]. Thermal stability is often the necessary type of stability evaluated for new MOFs because high thermal stability is a useful predictor of resistance to other stresses.

Mechanical stability of MOFs under vacuum or pressure is another important factor for MOF's industry and practical applications from an engineering perspective. Although extraordinary porosity and the very high surface area make MOFs desirable for absorption and other applications, they also make the MOFs inherently less mechanically stable. This instability can manifest itself as phase changes, partial collapse of pores or even amorphization, in response to mechanical loading. Grinding and ball milling often result in reduction or loss of MOF crystallinity and negatively affect its performance [61]. An under-appreciated source of MOF mechanical degradation is the capillary force exerted when removing strongly associated, pore-filling solvent molecules, especially water. This can easily be mistaken for hydrolytic degradation because the degradation products can appear identical [30]. Study on strategies to increase mechanical stability of MOFs has been rather limited. Recently a calculation work was done to rationalize the relationship between mechanical properties of MOFs and framework bonding topology and ligand structure [62]. It was concluded that the functional groups on the organic ligands could either enhance the mechanical stability through formation of a secondary network of non-bonded interactions or weaken the MOF by destabilizing the bonded network. Thus, it is important to design, test, and optimize functional groups that can synergistically match the secondary network with the bonding network of MOFs.

With sustained attentions on stable MOFs and the deep understanding of fundamental factors affecting structural stability, new MOFs with superior chemical and physical stability continue to be discovered currently. The ever-increasing number of stable MOFs has significantly expanded the application of MOFs. In addition to the conventional gas storage and separation, they have also been widely applied in catalysis, biomedicine, sensing, and other areas, which will be discussed in detail in the following sections.

Pore characters and surface area

The permanent and highly ordered porosity is one of the most prominent features of MOFs and provides the basis for their various functions. Most of MOFs developed thus far are microporous (pore diameter < 2 nm) in nature and have shown great adsorption capacities for various gases including hydrogen, carbon dioxide, and others. While high micropore volumes and large surface areas are desirable for many applications, such narrow pores do not allow for hosting large objects and anchoring molecular functionalities nor fast mass diffusion and transfer, thereby limiting their uses in storage, separation, catalysis, and drug delivery. For some of the newer applications such as catalysis and drug carrier, mesoporous MOFs (pore diameter 2–50 nm) and macroporous (pore diameter > 50 nm) MOFs are desirable [7,63]. The MIL-100(Cr) and MIL-101(Cr) are very famous cage-type mesoMOFs. In 2004, Férey et al. reported the synthesis and structure of MIL-100(Cr) for the first time and in 2005 MIL-101(Cr) was also reported by the same group [23,64]. A

number of strategies have been shown to be effective at constructing and tuning MOFs of large pore sizes. Elongation of the length of ligands is an apparent and effective way to do this [17,65]. The current record holder for the largest pores in MOFs is IR-MOF-74-XI with a staggering pore aperture of 98 Å (Fig. 5a) [17]. In principle, the linear extension of organic linkers tends to enhance the pore size of MOFs in a given network, but sometimes the pore diameter achievable in such MOFs is limited by interpenetration, a case of mutual growth of two or more networks in a structure where the networks are physically but not chemically linked. Thus the search of new mesoMOF materials with high surface areas remains a major challenge in the rapidly expanding field of MOFs. Recently supramolecular templating of hierarchically ordered MOFs has emerged as an alternative method [66]. The templates can be categorized as been hard, such as polystyrene [18,67–69], or soft, such as micelles [70], surfactants [71,72], block co-oligomer templates [73], and others. For example, Li et al. constructed Zr-based mesoporous MOFs with uniform mesochannels and crystallized microporous framework in a water-based system using amphoteric surfactants as templates (Fig. 5b) [72]. In addition, defect formation can be considered as a special way of templating to synthesize mesoporous MOFs [74–78]. For example, Cai and Jiang developed a versatile modulator-induced defect-formation strategy to realize the controllable synthesis of hierarchically porous MOFs (HP-MOFs) with high stability (Fig. 5c) [74].

In addition to pore size, the Brunauer–Emmett–Teller (BET) surface area and Langmuir surface area are also important for the functional applications of MOFs [79]. NU-110 holds the record for the highest surface area of any material reported so far (7140 m^2/g) [80]. Calculation indicates that the theoretical upper limit for MOF surface areas is around 14,600 m^2/g [80], so it remains a challenge to see how much of this can be realized experimentally.

Functional applications

Gas storage and separation

The highly ordered porous structures and large surface areas of MOFs make them ideal candidates for the storage of gases such as hydrogen, carbon dioxide, and methane. While large surface area is typically beneficial to gas adsorption and storage, the pore volume of MOFs is equally important because it provides the physical upper limit of how much gas can actually be stored. On the other hand, size and shape exclusion plays a crucial role in governing especially the separation process, which is often aided by the unique structural flexibility, resulting in an out-

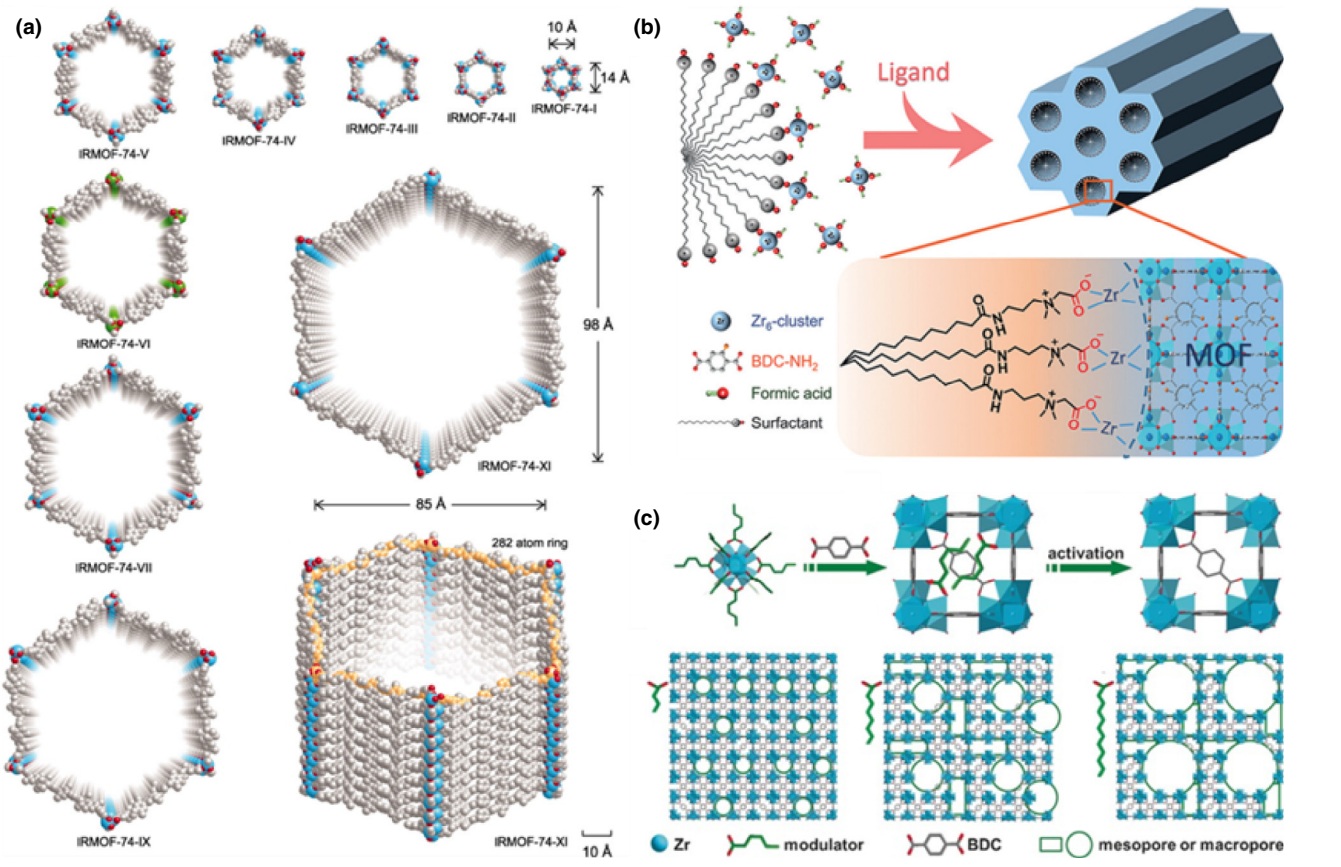

FIGURE 5

(a) Crystal structures of IRMOF-74 series [17]. Adapted with permission from Ref. [17]. Copyright 2012, the American Association for the Advancement of Science. (b) Schematic illustration for the construction of hexagonal mesoUiO-66-NH_2 MOFs [72]. Reproduced with permission from Ref. [72]. Copyright 2018, Wiley-VCH. (c) Schematic illustration of the synthesis of HP-UiO-66 with adjustable porosity [74]. Adapted with permission from Ref. [74]. Copyright 2017, Wiley-VCH.

standing molecular sieving effect. Additionally, the tunable structure of MOFs allows pre-functionalization of the pore surface, resulting in chemical separations that would have otherwise been difficult to achieve using conventional methods of separation used by chemical industries.

Gas storage

While MOFs are suitable for storing many different gases, hydrogen, methane, and carbon dioxide have received the most attention because of either their value as better alternative fuels or their environmental impact.

As a highly desired alternative to the non-sustainable carbon-based fuels, hydrogen burning generates no carbon dioxide and presents minimal pollution problem. Due to hydrogen's gaseous nature and low density, hydrogen storage is the key factor in deciding its practical usage as a fuel for transportation, stationary, and portable applications. Since the discovery of the first MOF (MOF-5) for hydrogen storage in 2003 by Yaghi and co-workers [81,82], MOFs have been extensively studied for hydrogen storage [83]. The interaction of MOFs with hydrogen molecules has been restricted to physisorption in which weak van der Waals forces are involved. The most useful measure for hydrogen storage capacity for MOFs is the interaction enthalpy between a MOF and H_2 molecule, i.e., the isosteric heat (Q_{st}) of hydrogen adsorption. It can be calculated from the hydrogen adsorption isotherms measured at two independent temperatures, most often 77 and 87 K by fitting the data to the Langmuir–Freundlich equation. The Q_{st} of most MOFs is in the range of 3–10 kJ/mol, but for practical applications at room temperature the value needs to be increased to 15–20 kJ/mol. Some strategies that have proven to improve Q_{st} include the incorporation of coordinatively unsaturated metal centers or aromatic benzene rings into MOFs, but so far good hydrogen storage capacity of MOFs has only been achieved at low temperature. The US Department of Energy has set the following goals for the onboard automotive hydrogen storage systems: 1.5 kWh/kg system (4.5 wt% hydrogen), 1.0 kWh/L system (0.030 kg hydrogen/L), and $10/kWh ($333/kg stored hydrogen capacity) by 2020 [84]. So far, the highest capacity of hydrogen at low temperature by MOF materials has been achieved with MOF-210 (17.6 wt% at 77 K and 80 bar) [85]. The capacity quickly diminishes when the temperature is raised, and the current record holder is $Be_{12}(OH)_{12}$(1,3,5-benzenetribenzoate)$_4$ (2.3 wt% at 298 K and 95 bar) [86]. Efficient hydrogen at ambient pressure is highly desirable, and the microporous copper-based MOF [Cu(Me-4py-trz-ia)]$_n$ (Me-4py-trz-ia^{2-} = 5-(3-methyl-5-(pyridin-4-yl)-4H-1,2,4-triazol-4-yl)isophthalate) holds the record of 3.07 wt% H_2 at 77 K and 0.1 MPa [87].

Although not as clean as hydrogen, natural gas, whose main component is methane, is an attractive fuel because it is naturally abundant and emits significantly less carbon dioxide and other toxic gases such as sulfur oxide than conventional liquid hydrocarbon fuels do. Adsorption of natural gas by a proper material would lower its working pressure, increase fuel density, and improve safe handling. Compared to the traditional adsorbents like zeolites and activated carbons with limited porosity and tunability, MOFs as a new class of materials have demonstrated superior performance for methane storage [88–91]. While maximum adsorption capacity is critical for the evaluation of a methane storage material, the working capacity, or deliverable capacity, is even more important for practical reasons. The working capacity is the amount of gas released when the pressure is reduced. It represents the amount of methane that can be actually utilized. To mimic the actual operation of natural gas fueled cars, methane uptake of MOFs has been measured at high storage pressures (35, 65, and 80 bar) and low pressure that mimics the emptied tank (5 bar) to determine their working capacity. Some top performing MOFs for methane storage are listed in Table 1.

As the primary anthropogenic greenhouse gas, elevated concentrations of atmospheric CO_2 could lead to a rise in the average temperature of the Earth and cause disastrous environmental problems including acidification of oceanic water. Carbon dioxide generally forms stronger intermolecular interactions with open metal sites and other functionalities of MOFs than hydrogen does, and this has been harvested for effective carbon storage [99]. MOFs are capable of adsorbing a large amount of CO_2 with their large surface area. Currently MOF-200 and MOF-210 hold the record for holding ~71 wt% CO_2 at 298 K and 50 bar, which is highest reported value for all porous materials [85]. The CO_2 storage capacity of MOFs at ambient pressure is more relevant to flue gas CO_2 capture, and the capacity is affected both by surface area and more importantly by adsorbent–CO_2 interactions. The current best-performing MOF at ambient pressure is Mg-MOF-74 [Mg_2(DOT); DOT: 2,5-dioxidoterephthalate], a framework with open Mg^{2+} sites, which has a high CO_2 storage capacity of 35.2 wt% at 298 K and 1 bar [100]. The open metal centers are essential for the high capacity.

Gas sorption and separation

While gas storage is focused on the storage of a pure gas, gas sorption and separation require MOF to have highly selective adsorption of a specific gas from a mixture. The selective adsorption of carbon dioxide is called carbon caption and is particularly important for precombustion CO_2 capture from H_2, precombustion CO_2 capture from CH_4, and postcombustion CO_2 capture from flue gas [101,102]. Steam reforming of methane or natural gas provides a mixture of hydrogen and carbon dioxide and is the largest source of global hydrogen production. Complete removal of carbon dioxide is critical for improving the fuel quality of hydrogen. Carbon dioxide is also the major impurity component in natural gas and needs to be removed prior to combustion for fuel efficiency. Burning of all fossil fuels in atmosphere generates flue gas which typically contains ~15% CO_2, more than 67% N_2, and other minor gases. Capture of CO_2 from all these gas mixtures is challenging because the low partial pressure of CO_2 as a minor component would significantly lower its adsorption by MOF. On top of that, the selective adsorption of CO_2 but no other components must be achieved. To improve both the adsorption capacity as well as selectivity of CO_2 against other gases, introduction of open metal sites and aliphatic amine functionalities into MOFs has proven to be effective. Under conditions similar to those of flue gas, Mg-MOF-74 is the best performing CO_2 adsorbent among all MOFs and other porous materials with 23.6 wt% capacity at 0.1 atm and 296 K [103], and the open Mg^{2+} centers are essential for the high affinity for CO_2. IRMOF-74-III-CH_2NH_2 contains both open Mg^{2+} centers and amine groups and can efficiently capture CO_2 (3.2 mmol

TABLE 1

Volumetric methane storage performance of top-performing MOFs at room temperature.

MOF	Open Metal Sites (OMSs)	BET (m^2/g)	Total uptake at 5/35/65/80 bar (cm^3/cm^3)	Working capacity for 35/65/80 bar (cm^3/cm^3)	Q_{st} (KJ/mol)	Refs.
MAF-38	N/A	2022	76/226/263/273	150/187/197	21.6	[92]
Co(dbp)	N/A	2911	6/161/203/N.A.	155/197/N.A.	13	[93]
MOF-5	N/A	3961	32/150/214/235	118/182/203	12.3	[90]
MOF-520	N/A	3290	37/162/215/231	125/178/194	13.6	[94]
HKUST-1	Cu	1850	77/227/267/272	150/190/200	17.0	[90,91]
UTSA-76a	Cu	2820	60/211/257/N.A.	151/197/N.A.	15.4	[95]
Ni-MOF-74	Ni	1350	115/230/260/267	115/145/152	20.6	[90]
PCN-14	Cu	2000	79/202/239/250	123/160/171	17.6	[90]
UTSA-75a	Cu	2838	59/205/251/N.A.	146/192/N.A.	14.93	[96]
Al-soc-MOF-1	Al	5585	21/127/197/222	106/176/201	11	[97]
Cu-tbo-MOF-5	Cu	3971	41/151/199/216	110/158/175	20.4	[98]

of CO_2 per gram at 800 Torr) in the presence of water [104]. It is interesting to note that CO_2 uptake takes place at the linker amine sites, while the open magnesium sites are not accessible under dry or humid conditions. Apparently, the hidden Mg^{2+} centers render the MOF water stable. McDonald et al. studied a series of mmen-M_2(dobpdc) (mmen = *N,N′*-dimethylethylenediamine, M = Mg, Mn, Fe, Co, Zn, dobpdc^{4-} = 4,4′-dioxidobiphenyl-3,3′-dicarboxylate) and demonstrated that CO_2 can be cooperatively inserted into the metal–amine bonds upon adsorption [105]. It was found that CO_2 adsorption isotherms varied with different metal used and the MOFs can be fine-tuned to suit the separation of CO_2 of different concentration. Hydrazine has higher amine content than any alkyl amines and can be well accommodated in the pores of Mg-MOF-74. Liao et al. thus synthesized [Mg_2(dobdc)(N_2H_4)$_2$] and showed that at 0.4 mbar, corresponding to the CO_2 concentration in air, the hydrazine-loaded MOF showed high CO_2 uptake of 3.89 mmol·g^{-1} or 4.58 mmol·cm^{-3}, drastically surpassing Mg-MOF-74 (0.09 mmol·g^{-1} or 0.08 mmol·cm^{-3}) and other CO_2 absorbent [106]. It is noteworthy that the hydrazine incorporation not only increases the CO_2 affinity but also makes the MOF almost waterproof. In addition to open metal centers and amine groups, inorganic ions like SiF_6^{2-} can form favorable electrostatic interactions with CO_2 to increase adsorption. Nugent et al. synthesized a series of SIFSIX MOFs ([M(dpa)$_2$(SiF_6)]$_n$, M = Cu^{2+} and Zn^{2+}, dpa = 4,4′-dipyridylacetylene) with high CO_2 sorption selectivity over N_2, H_2 and CH_4 in the presence of moisture [107].

Since the porosity of MOFs can be tuned to suit the specific size of guest molecules and functional groups can be added either during or after the MOF construction, MOFs have also been explored for other separations including acetylene/ethylene, xenon/krypton, branched/linear alkanes, olefins, toxic gases like CO and NH_3, and others [9,108–113]. Peng et al. used a soft-physical process to exfoliate the layered MOF [Zn_2(benzimidazole)$_4$]$_n$ to generate 1-nanometer-thick sheets with large lateral area and high crystallinity [114]. The resulting molecular sieve membranes achieved H_2 permeance of up to 3760 gas permeation units (GPUs) with H_2/CO_2 selectivity up to 291. The copper-based SIFSIX (SiF_6^{2-}) MOFs were also found to have high adsorption capacity (2.1 mmol/g at 0.025 bar) and selectivity (39.7–44.8) for acetylene over ethylene at ambient conditions [115]. Computations and experiments revealed that primary binding sites were necessary for recognizing acetylene, whereas precisely controlled pore sizes and spacing were essential to achieve synergistic binding to multiple sites to form gas clusters. 1,3-Butadiene is one of the most produced chemical products worldwide and is mainly used to make synthetic rubber. It is typically purified by distillation from a mixture containing a number of other C4 hydrocarbons (1-butene, isobutene, and butane) which is tedious and energy consumptive. Liao et al. synthesized a hydrophilic MOF [Zn_2(btm)$_2$]$_n$ (H_2btm = bis(5-methyl-1H-1,2,4-triazol-3-yl)methane) with both isolated cavities and continuous channels [116]. The quasi-discrete pores induced conformational changes in flexible guest molecules and resulted in selective adsorption of other C4 hydrocarbons over 1,3-butadiene. As such 1,3-butadiene could be purified (≥99.5%) at ambient conditions without undergoing undesirable polymerization.

Heterogeneous catalysis

As one of the earliest demonstrated applications of MOFs [117], catalysis with MOFs presents rapid development in the past two decades [10,118–128]. In view of structure, the domains in MOFs are similar to the traditional homogeneous catalysts, which are related to soluble transition metal complexes, while MOFs are actually heterogeneous and insoluble in different solvents. On the other hand, the periodic structure enables MOFs to disperse active sites uniformly throughout the framework. Moreover, the highly ordered pores and channels within MOFs facilitate the accessibility of active sites and the transport of substrates and products. MOFs can thus be regarded to have the dual advantages of both heterogeneous and homogeneous catalysts.

Compared to the traditional porous catalysts such as zeolites and activated carbons, MOFs have much more diversified structures with highly tunable pore sizes (usually 0–3 nm, up to 9.8 nm) ranging from microporous to macroporous. The uniform pore size and shape allows the accessibility of reaction substrates with specific shape and size, thus making it possible to differentiate substrates which are similar to each other. MOFs typically have high surface areas from 1000 to 7000 $m^2\,g^{-1}$ which favor the adsorption and enrichment of substrate molecules around the active sites, further benefiting the subsequent activation and catalytic conversion.

The metal ions in MOFs are usually coordinated with organic ligands and solvent molecules, the latter of which can be readily removed by heating or vacuum with retained framework structures, creating the coordinatively unsaturated metal sites (CUSs). The CUSs can act as typical Lewis acid centers for accepting electrons from the substrates and promoting their conversion to products. Besides, functional groups on organic linkers can also be tailored for heterogeneous catalysis. There is a variety of functional groups serving as active sites for catalysis. The active functional groups can be linked to the MOF ligands, thereby resulting in a stable catalytic system. The catalytic centers involved in pristine MOFs are usually limited to CUSs and the active sites on the linkers, which limit pristine MOFs to a certain scope of catalytic reactions. Fortunately, there are at least two solutions to circumvent this problem. The first solution is functionalized modification by grafting desired active sites onto either metal ions/clusters or organic linkers by the multivariate approach or postsynthetic modification. The second is pore confinement and encapsulation. Some MOFs have pores big enough to accommodate various catalytically active species like inorganic nanoparticles, metal complexes, small organic molecules, or even enzymes. The host–guest system can act as a complete catalytic system.

Traditionally, MOFs have been widely explored as heterogeneous catalysts for various organic reactions. In recent ten years, MOFs and MOF-based composites have also shown excellent catalytic activities for energy-related applications such as photocatalysis and electrocatalysis, which will continue to be one research frontier of MOFs in the future [129–133].

MOF catalysts for heterogeneous organic reactions

Active catalytic centers in MOFs can be generated in three different locations within the structure of MOFs, i.e., at the metal centers, at the organic linkers, and at the pore space. Metal centers can be readily generated in MOFs through removal of coordinated solvent molecules. For example, the classical HKUST-1 gave open Cu^{2+} sites upon the removal of coordinated water molecules, exhibiting Lewis acid activity in the cyanosilylation of benzaldehyde and the isomerization of terpene derivatives [134,135]. MIL-101(Cr), composed of trimeric chromium(III) octahedral clusters interconnected by 1,4-benzenedicarboxylate (BDC) anions, exerted Lewis acidity upon the removal of the terminally coordinated H_2O molecules for better activity than HKUST-1 in the cyanosilylation of aldehydes, because of the stronger Lewis acidity of Cr(III) [136]. Horike et al. reported a 3D porous $Mn_3[(Mn_4Cl)_3BTT_8(CH_3OH)_{10}]_2$ (H_3BTT = 1,3,5-benzenetris(tetrazol-5-yl)), built from chloride-centered square-planar $[Mn_4Cl]^{7+}$ units linked by BTT^{3-} ligands with 7 and 10 Å pores [137]. Owing to the exposed Mn(II) centers, the MOF presented good catalytic activity for the cyanosilylation of benzaldehyde (Fig. 6a). In addition to the pristine metal nodes, nickel ions were uniformly dispersed in Zr-based MOF NU-1000 through atomic layer deposition (ALD) and the resulting sintering-resistant single-site Ni catalyst turned out to be one of the best available hydrogenation catalysts based on earth-abundant elements with high activity, long-term stability, and excellent regenerability [138]. The catalyst was effective for both hydrogenation and ethylene oligomerization reactions.

Catalytically active functional groups can be incorporated into the organic linkers for MOF construction. For example, the sulfonic acid group ($–SO_3H$) can be grafted onto the aromatic linker to fabricate MOFs such as MIL-101(Cr). Akiyama et al. prepared MIL-101(Cr) containing partially protonated $–SO_3Na$ group using 2-sulfoterephthalate in the presence of HCl [139]. With the strong Brønsted acid site on its pore surface, this MOF showed high activity in the catalytic cellulose hydrolysis. Lewis basic functional groups like pyridyl, amide and amino group can also be incorporated in organic linkers of MOFs to generate basic catalyst. Seo et al. synthesized a homochiral MOFs D-POST-1 with 1D channels using the pyridyl group functionalized organic linker [140]. Bearing half of pyridine groups in channels, the framework possessed the basic sites for the transesterification of 2,4-dinitrophenyl acetate. In addition to direct incorporation of functional groups, post-synthetic modification can also result in additional catalytic centers. A molecular nickel complex was anchored to a mesoporous MOF (Ni@Fe-MIL-101) via post-functionalization, generating a very active and reusable catalyst for the liquid-phase ethylene dimerization to selectively give 1-butene, the activity of which was better than the corresponding molecular nickel diimino complexes (Fig. 6b) [141]. The bipyridyl and phenanthroline-containing UiO MOFs were used as templates to incorporate cobalt catalysts through postsynthetic metalation (Fig. 6c) [142]. The resulting catalysts showed high activity, robustness, and recyclability for a wide range of reactions including alkene hydrogenation and hydroboration, aldehyde/ketone hydroboration, and arene C–H borylation.

In addition to the catalysis at metal nodes and organic linkers of MOFs, incorporation of catalytically active complexes as guests into MOF pore spaces has been a widely adopted approach to generate MOF catalysts so far. This approach benefits from the free choice of any catalytic centers and a vast number of MOFs that can be chosen as templates/hosts. Using an anionic bio-MOF-1 as template, positively charged Co^{2+} ions were first exchanged into its framework by electrostatic interaction followed by reaction with 1,2-dicyanobenzene to form cobalt(II) phthalocyanine (Co–Pc) complex within the MOF's nanospaces via confinement effect (Fig. 6d) [143]. The resultant Co-Pc@bio-MOF-1 showed superior activity to catalyze styrene epoxidation reaction than the homogeneous Co-Pc counterpart. The ruthenium complex ($^{t\text{Bu}}$PNP)Ru(CO)-HCl ($^{t\text{Bu}}$PNP = 2,6-bis((di-*tert*-butylphosphino)methyl)-pyridine) was encapsulated in UiO-66 through a solvent-dependent, aperture-opening process resulting from dissociative linker exchange reactions in the MOF [144]. Compared to the corresponding homogeneous catalyst, [Ru]@UiO-66 showed improved recyclability, stability, and resistance to catalyst poisoning for the hydrogenation of CO_2 to formate.

In addition to metal complexes, metal nanoparticles (MNPs) are an important class of MOF guests with diverse functions, particularly in catalysis [145,146]. Platinum nanoparticles were sandwiched between an inner core and an outer shell composed of MIL-101 to generate a selective catalyst for the hydrogenation of α,β-unsaturated aldehydes to yield unsaturated alcohols [147]. MIL-101 served as an effective selectivity regulator of Pt nanoparticle while maintaining efficient reactant and product transport owing to the porous nature of the material. Without the MOF, the Pt catalysts alone would selectively hydrogenate the

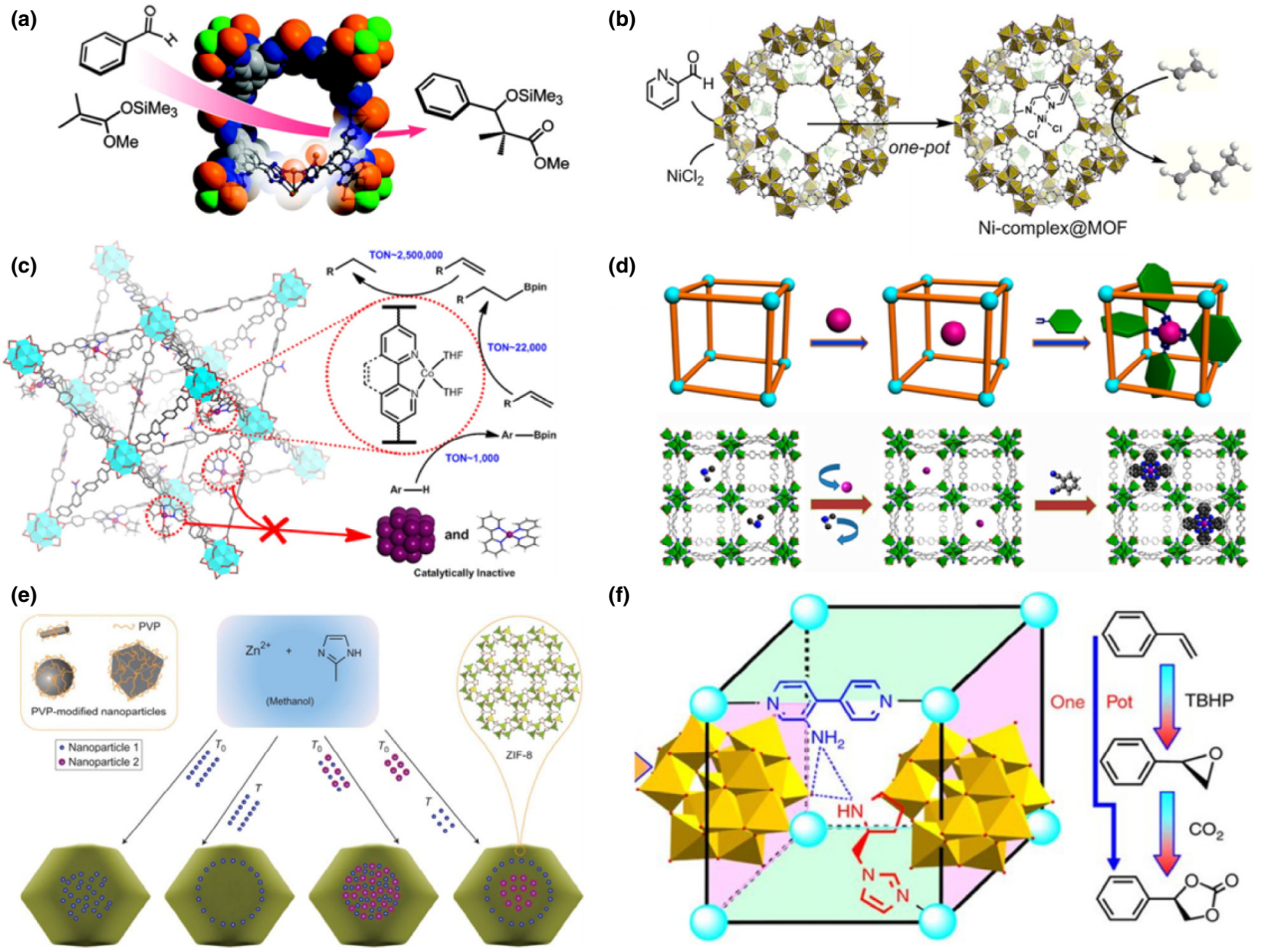

FIGURE 6

(a) Catalysis of the benzaldehyde cyanosilylation reaction over $Zn_3[(Mn_4Cl)_3BTT_8(CH_3OH)_{10}]_2$ [137]. Adapted with permission from Ref. [137]. Copyright 2008, American Chemical Society. (b) Schematic illustration of the synthesis of Ni(II) complex@Fe-MIL-101 for selective ethylene dimerization [141]. Adapted with permission from Ref. [141]. Copyright 2013, American Chemical Society (c) Schematic showing the beneficial effects of active site isolation in MOFs [142]. Reproduced with permission from Ref. [142]. Copyright 2013, American Chemical Society. (d) The *de novo* assembly of Co-Pc@bio-MOF-1 [143]. Reproduced with permission from Ref. [143]. Copyright 2014, American Chemical Society. (e) The controlled encapsulation of nanoparticles inside the controlled position of ZIF-8 particles [151]. Adapted with permission from Ref. [151]. Copyright 2012, Nature Publishing Group. (f) The design concept of achieving a tandem catalyst [167]. Adapted with permission from Ref. [167]. Copyright 2015, Nature Publishing Group.

carbon–carbon group in preference to the carbon–oxygen group because the process is thermodynamically favored. The sandwich catalyst overturned this selectivity. An et al. used both the bipyridyl ligand and $Zr_6(\mu_3\text{-}O)_4(\mu_3\text{-}OH)_4$ sites in UiO-bpy MOF to anchor the ultra-small Cu/ZnO_x nanoparticles, preventing the agglomeration of Cu NPs and phase separation between Cu and ZnO_x [148]. The resultant Cu/ZnO_x@MOF catalysts showed high activity with a space–time yield up to 2.59 $g_{MeOH}\ kg_{Cu}^{-1}\ h^{-1}$, 100% selectivity and high stability. The controlled spatial distribution of MNPs within MOFs is a challenging problem. One interesting strategy is to use metal oxide both as support to load MNPs and as a sacrificial template to grow MOFs [149]. Pt NPs located near the surface of the MOF layers (Pt@ZIF-8-'sur') was synthesized and showed exclusive catalytic activity for the hydrogenation of linear hexene but not the cyclic cyclohexene. Such selectivity was rare in other related Pt NP-based catalysts. The incorporation of catalytic centers into MOFs can also be achieved by modifying the conditions for MOF synthesis. By adding glycine in MIL-101 synthesis, Lewis acid and base-like chromium hydroxide sites were generated in situ in MIL-101 and the material effectively catalyzes glucose isomerization in ethanol with comparable efficiency to the obtained by that Sn-containing Lewis acidic zeolites [150]. Lu et al. reported a general approach for encapsulation of the polyvinylpyrrolidone (PVP)-stabilized NPs with various sizes, shapes, and compositions into ZIF-8 which can be extended to other nanostructured materials. (Fig. 6e) [151]. The spatial distribution of incorporated NPs within ZIF-8 crystals was also controllable by their addition sequence. The Pt/PVP/ZIF-8 catalyst showed exclusive selectivity for *n*-hexene over its constitutional isomer *trans*-2-hexene. Not limited to metal nanoparticles, phosphotungstic acid (PTA) was recently encapsulated within NU-1000, a Zr-based MOF, and showed remarkable catalytic activity for the *o*-xylene isomerization and disproportionation at a high temperature of 523 K [152]. Using a simple PDMS coating method, surface hydrophobic Pd/UiO-66@PDMS was successfully synthesized [153].

Remarkably, the hydrophobic PDMS coating facilitated the enrichment of hydrophobic substrates and thereby promoted interaction with Pd sites. As a result, Pd/UiO-66@PDMS exhibited significantly improved catalytic efficiency in various reactions and enhanced recyclability compared to the pristine Pd/UiO-66. By the integration of Pt nanocrystals and porphyrinic MOFs, PCN-224(M), Chen et al. reported a Pt/PCN-224(Zn) composite exhibiting excellent catalytic performance in the photooxidation of aromatic alcohols, based on a synergetic photothermal effect and singlet oxygen production of both Pt NCs and PCN-224(Zn) [154].

MNPs/MOF composites can also be employed to realize synergetic catalysis and cascade reactions. Chen et al. successfully synthesized bimetallic PdAg alloy NPs (1.5 nm) in the cavities of MIL-101 [155]. The obtained PdAg@MIL-101 presented great catalytic activity and selectivity toward one-pot cascade reactions, in which MIL-101 offered Lewis acidity and PdAg afforded selective hydrogenation activity. Yang et al. also reported the synthesis of Pd@MIL-101 composite with tiny Pd NPs, which exhibited excellent catalytic performance in tandem dehydrogenation of ammonia borane and reduction of nitro compounds [156]. Similar to nanoparticle, ionic liquid can also be incorporated in MOFs. Ding et al. confined imidazolium-based poly(ionic liquid)s (denoted as polyILs) into MIL-101 via in situ polymerization and the resultant polyILs@MIL-101 exhibited good catalytic performance for the cycloaddition of CO_2 at subatmospheric pressure in the absence of any cocatalyst [157].

In addition, MOF-derived single-atom catalysts (SACs), with the maximized utilization of metal atoms, have also shown ultrahigh efficiency and selectivity in various organic reactions. Sun et al. reported a facile method to construct a single-atom cobalt catalyst based on ZnCo-ZIF materials, which displayed high activity and selectivity (>99%) for selective hydrogenation of nitrobenzene to aniline under mild conditions [158]. Very recently, Wei et al. discovered an unexpected conversion of noble metal nanoparticles into thermally stable single atoms at above 900 °C in an inert atmosphere. The single-atom Pd catalyst exhibited even better activity and selectivity than Pd nanoparticles for semihydrogenation of acetylene [159]. The examples above demonstrate the great potentials of MOF-based SACs for heterogeneous catalytic processes.

Asymmetric catalysis is one specialized and highly practically useful area in which MOFs have turned out to have unique advantages [160–162]. The first reported MOF for asymmetric catalysis is D-POST-1 which contained a chiral ligand derived from D-tartaric acid, presenting 8% enantiomeric excess (ee) for transesterification reaction [140]. Since then a great number of chiral MOFs have been developed and the ee values have been improved. Wu et al. used a chiral bridging ligand containing two orthogonal functional groups [163]. The primary bipyridyl group can complex with Cd^{2+} to form the homochiral MOF, and the secondary 2,2′-dihydroxy group was used to react with Ti^{4+} to generate catalytic centers. The MOF system effectively catalyzed the $ZnEt_2$ addition to aromatic aldehydes with up to 93% ee, comparable to the corresponding chiral homogeneous catalyst BINOL/Ti(O^iPr)$_4$. A different approach to generate chiral MOF catalyst is to postsynthetically attach chiral ligand to an achiral MOF. Banerjee et al. demonstrated that L-proline-based chiral ligands can be attached to the open metal coordination sites of MIL-101, and the resulting chiral MOF showed remarkable catalytic activities (60–90% yields, 55–80% ee) in asymmetric aldol reactions, including much higher enantioselectivity than the chiral ligands themselves [164]. Cui and coworkers developed a homochiral biphenol-based MOF decorated with chiral dihydroxyl auxiliaries, which can be partially deprotonated by *n*-butyllithium [165]. The MOF catalyst outperformed the homogeneous counterpart in asymmetric cyanation of aldehydes with up to >99% ee. Cui and coworkers also utilized two mesoporous MOFs bearing free carboxylic acid groups as a host to encapsulate chiral amines through acid-base interactions [166]. The modified MOFs turned out to be efficient for the asymmetric direct aldol reactions. Duan and coworkers demonstrated that tandem MOF catalyst can be made by combining multiple catalytic centers into the MOF structure (Fig. 6f) [167]. The chiral MOF catalyzed the tandem epoxidation and then cyclic carbonate formation of olefins in a highly enantioselective manner (25% to quantitative yield, up to 96% ee).

Photocatalytic reactions

Photocatalysis is one fast growing field for catalytic application of MOFs recently [10,168–172]. The three most important parameters of a photocatalyst are the spectrum-responsive range, the effective separation of electrons and holes, and the redox reaction efficiency of the charge carriers. MOFs can present semiconductor-like behavior in that the organic ligands provide the highest occupied molecular orbital (HOMO) and the metal nodes provide the lowest unoccupied molecular orbital (LUMO). Irradiation of MOFs by a suitable light source typically results in a ligand-to-metal charge-transfer (LMCT) process in which electrons from the ligands are transferred to the metal nodes, resulting in the electron-hole separation [173]. Given the theoretically unlimited number of organic ligands, improving the photoresponsive range of ligands has been an important approach to tune the activity of MOF photocatalysts. MOF-based photocatalysts have been widely used for photocatalytic organic pollutant degradation, various organic reactions, hydrogen/oxygen production from water splitting, and reduction of CO_2. The early work in this area utilized amine-functionalized MOFs and extended the photoresponsive range from the typical UV to the visible range, however it was typically within the short-wavelength range of less than 450 nm. Incorporation of other functional units like the strong visible light-absorbing porphyrins further extends the photoresponsive range [174]. In addition to ligand modification, other materials including semiconductors, plasmon polariton-responsive metals, and upconversion nanoparticles (UCNPs) have been incorporated in MOFs to improve photocatalytic activity [175,176]. Lastly, introduction of co-catalysts also could boost the activity of the whole system by inhibiting the combination of electrons and holes as well as providing additional active sites. For example, platinum as a co-catalyst could trap electrons and facilitate the photocatalytic hydrogen production [175]. One significant challenge of MOF catalysts is most studies so far have focused on half reaction like hydrogen production from water, and a sacrificial agent is needed to complete the other half reaction. Most recently, Liu et al. tried to couple photocatalytic H_2 production with organic

oxidation transformation by hole oxidation to give value-added products in the absence of any sacrificial agent [177]. The stability of MOFs also must be addressed especially when the photocatalytic reaction is carried out in water. In this section, we will focus on the latest developments of MOFs in light-driven energy conversion reactions including organic pollutant degradation, organic reactions, water splitting, and CO_2 reduction.

The MOF-catalyzed photocatalytic organic pollutant degradation has been studied for dyes such as methylene blue, methyl orange, cresol red, coomassie brilliant blue and small molecules such as thiophene and phenol [178]. It was common for such organic molecules to bear chromophores or conjugated systems to facilitate visible light absorbance. In addition to the organic pollutants degradation, various organic reactions have been shown to be subject to photocatalysis by MOF catalysts. The photoredox catalyst $[SiW_{11}O_{39}Ru(H_2O)]^{5-}$ was incorporated into the pores of copper(II)-bipyridine MOFs [179]. Direct Cu^{II}–O–W(Ru) bridges and the two metal centers synergistically catalyzed the C–C coupling of acetophenones and *N*-phenyltetrahydroisoquinoline with excellent conversion and size selectivity. A series of porphyrin-based MOFs were constructed, of which ZJU-18 ($[Mn_5Cl_2(MnCl\text{-}OCPP)(DMF)_4(H_2O)_4]\cdot 2DMF\cdot 8CH_3COOH\cdot 14H_2O$, H_8OCPP = 5,10,15,20-tetrakis(3,5-bis carboxylphenyl)porphyrin) catalyzed highly efficient and selective oxidation of ethylbenzene to acetophenone in quantitative yield and a turnover number of 8076 after 48 h [180]. A number of amine-containing MOFs have been shown to be effective photocatalysts either by themselves or after suitable modification. The zirconium centers in amine-functionalized UiO-66-NH_2 turned out to be effective visible-light photocatalyst for selective aerobic oxygenation of various organic compounds including alcohols, olefins, and cyclic alkanes [181]. The reaction was substrate- and solvent-dependent, thus alcohols including benzyl alcohol, cyclohexanol, and hexyl alcohol and the cyclic alkane cyclohexane were oxidized to the corresponding aldehydes and ketones with 100% selectivity. Using the same MOF, CdS nanorods were decorated on the surface of UiO-66-NH_2 through photodeposition at room temperature, presenting considerable photocatalytic activity for oxidizing various alcohol substrates.[182]. It was assumed that charge injection from CdS into UiO-66-NH_2 led to efficient charge separation. The amine-functionalized NH_2-MIL-125(Ti) demonstrated photocatalytic activity for the aerobic selective oxidation of amines to imines under visible light irradiation [183]. Depending on the structure of substrates, the conversion ranged from 41% to 100%, and the selectivity ranged from 45% to 93%. NH_2-MIL-125(Ti) was post-synthetically functionalized with the dye molecule methyl red to improve light absorption over a wide range of the visible spectrum and showed enhanced photocatalytic oxidation activity for oxidizing benzyl alcohol into benzaldehyde [184]. Titanium oxide (TiO_2) is considered as green catalyst for many different transformations. It was incorporated into mesoporous HKUST-1 to give a composite catalyst, which selectively oxidize benzylic alcohols into the corresponding carbonyl compounds [185]. Primary and secondary benzylic alcohols containing both electron-rich and electron-poor substituents were tolerated, and high selectivity (93–99%) is achieved with moderate to high conversions (32–100%). In addition to inorganic nanomaterials which have been widely investigated for MOF catalysis, organocatalysts L- or D-pyrrolidin-2-ylimidazole (PYI) were incorporated into a zinc-based MOF to generated two enantiomers Zn–PYI1 and Zn–PYI2, in which 4,4′,4″-tricarboxyltriphenylamine (H_3TCA) ligands were capable of initiating photoinduced electron transfer processes [186]. The homochiral MOFs catalyzed the light-driven asymmetric α-alkylation of aliphatic aldehydes in a heterogeneous manner, resulting in good conversion (61–85%) and high selectivity (78–92% ee) (Fig. 7a). The enantiomeric selectivity of the MOF catalyst showed dramatic improvement to that of the corresponding catalyst without MOF (~20% ee), attributing to the well-defined structure of the composite.

Water splitting contains two half reactions, water reduction which generates hydrogen and water oxidation which generates oxygen. The hydrogen generation with MOF photocatalysts has been predominantly investigated due to the commercial and environmental value of hydrogen as a clean fuel. By incorporating the photosensitizer $Ru(bpy)_3^{2+}$ into the porous MOF $[Ru_2(p\text{-}BDC)_2]_n$ (p-BDC = *p*-benzenedicarboxylate), Kataoka et al. successfully realized the photoreduction of water to H_2 [187]. The water stable Zr-MOF, UiO-66, can serve as a photocatalyst for hydrogen production in a mixed solution of methanol and water under UV light irradiation. The subsequent introduction of $–NH_2$ group can expand absorption to visible region and the catalytic activity is significantly increased [188]. Porphyrins bear a wide absorption covering almost the whole range of visible light and have become a recent favorite organic motif to construct photoresponsive MOFs. Fateeva et al. constructed a water-stable Al-porphyrinic MOF as a photocatalyst for hydrogen generation from water splitting under visible light irradiation with a turnover number of 8.16 and a quantum yield of 4.82% (Fig. 7b) [174]. Based on the ligand 4′-(3,5-dicarboxyphenyl)-4,2′:6′,4″-terpyridine (DCTP), a semiconductive MOF ($[Cu^{I}Cu^{II}_2\text{-}(DCTP)_2]NO_3\cdot 1.5DMF)_n$ with a narrow band gap of 2.1 eV was generated [189]. The MOF exhibited a good band alignment with water and it could catalyze hydrogen production from water based on the photogenerated electrons under UV/Vis light in the absence of photosensitizers. Pt nanoparticles of 2–3 nm and 5–6 nm in diameter were loaded into UiO type MOFs built from Ir-phosphor-derived linear dicarboxylate ligands through MOF-mediated photoreduction of K_2PtCl_4 [190]. The Pt@MOF assemblies turned out to be efficient photocatalysts for hydrogen production with both higher turnover frequencies and higher turnover numbers than those of the homogeneous analogs. The facile electron transfer from the photoreduced Ir phosphor to the entrapped Pt nanoparticles resulted in the boost of catalytic activity. The location of Pt nanoparticles relative to the MOF host played important roles in the performance of the photocatalyst for hydrogen production [191]. The Pt@UiO-66-NH_2 greatly shortened the electron-transport distance, thus facilitating electron–hole separation and resulting in much higher efficiency (257 $\mu mol\cdot h^{-1}\cdot g^{-1}$) than that of Pt/UiO-66-NH_2 (50 $\mu mol\cdot h^{-1}\cdot g^{-1}$). Zhou et al. immobilized a Pt complex in 2,2′-bipyridine-based MOF-253 using a post-synthesis modification strategy [192]. The functionalized MOF-253-Pt ($Al(OH)(bpydc)\cdot 0.5PtCl_2$) served both as a photosensitizer and a photocatalyst for hydrogen evolution under visible-light

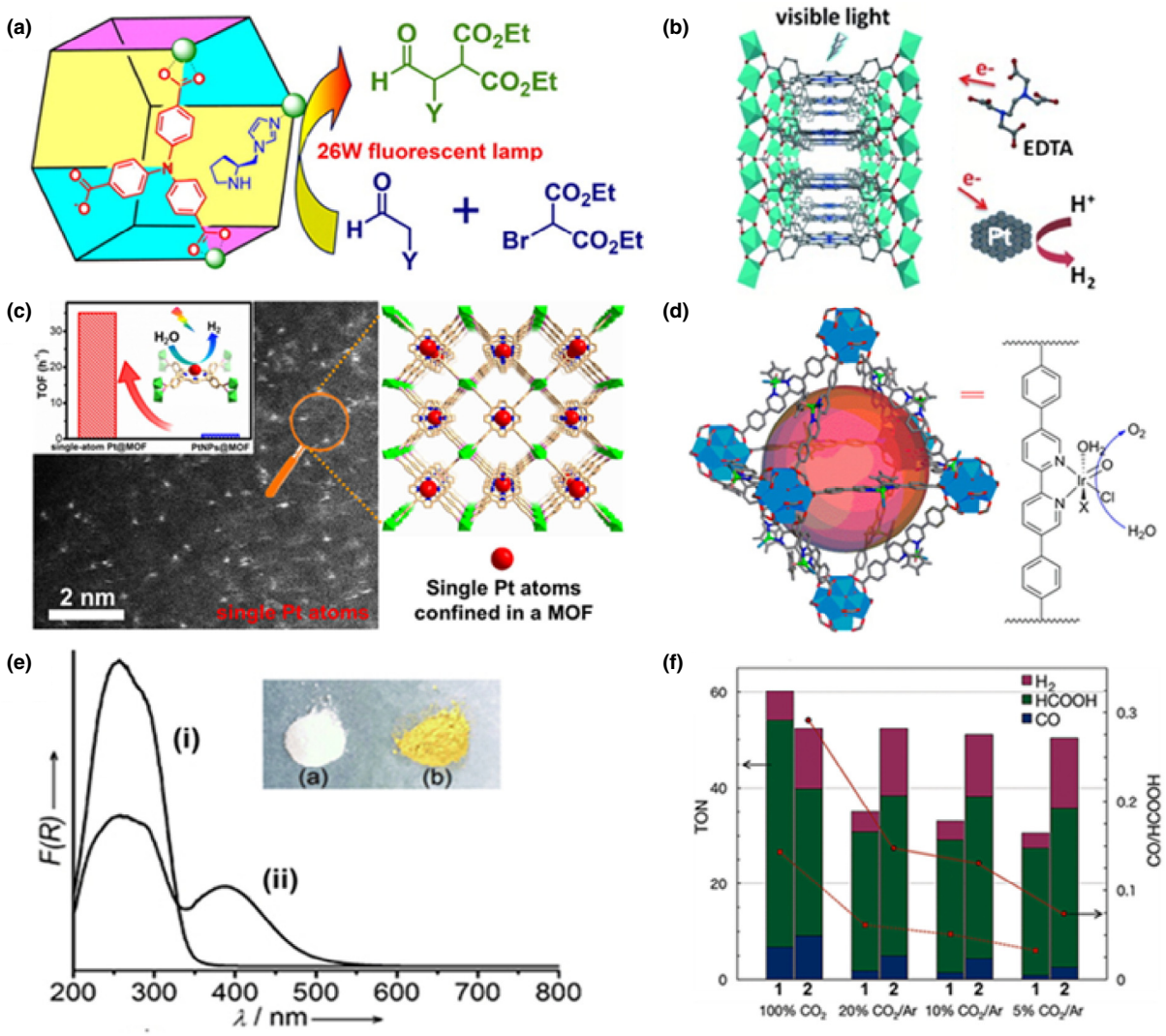

FIGURE 7

(a) Schematic representation of Zn-PYI1 for photocatalytic α-alkylation reaction upon light excitation [186]. Reproduced with permission from Ref. [186]. Copyright 2012, American Chemical Society. (b) Proposed photocatalytic H_2 generation using Al-porphyrinic MOF in the presence of EDTA under visible light irradiation [174]. Adapted with permission from Ref. [174]. Copyright 2012, Wiley-VCH. (c) Schematic illustration showing single Pt atoms confined into Al-TCPP for photocatalytic hydrogen production [197]. Reproduced with permission from Ref. [197]. Copyright 2018, Wiley-VCH. (d) Photocatalytic oxygen evolution of Zr-based MOF with (bpy-dc)Ir(H_2O)$_2$XCl as an active water oxidation catalyst [201]. Reproduced with permission from Ref. [201]. Copyright 2012, American Chemical Society. (e) UV/Vis spectra of i) MIL-125(Ti) and ii) NH_2-MIL-125(Ti) [206]. Adapted with permission from Ref. [206]. Copyright 2012, Wiley-VCH. (f) Photocatalytic CO_2 reduction with [Ru^{II}(bpy)(terpy)(CO)](PF$_6$)$_2$ (1) and PCP-Ru^{II} composite (2) [210]. Adapted with permission from Ref. [210]. Copyright 2016, Wiley-VCH.

irradiation and showed five-fold enhanced activity compared to that of the corresponding complex, attributing to the short-distance Pt/Pt interaction in the framework. Han et al. introduced 2,5-bis(methylthio)terephthalate (BDC-(SCH$_3$)$_2$) into the lattice of MIL-125 via solvent-assisted ligand exchange, and the MOF was further decorated with Pt co-catalyst [193]. Using triethanolamine as the sacrificial reagent, the hybrid x%-MIL-125-(SCH$_3$)$_2$ catalyzed hydrogen production at a rate of 3814.0 μmol·g^{-1}·h^{-1} with a high quantum yield (8.90 %) at 420 nm. In a one-pot hydrothermal process, Li et al. combined $TiCl_4$ and 1-hydroxyethylidene-1,1-di phosphonic acid (HEDP) in the presence of cationic surfactant cetyltrimethylammonium bromide (CTAB) as well as anionic polymer poly(acrylic acid) (PAA) to make mesoporous MOF (HM-TiPPh) as a hydrogen-producing photocatalyst [194]. Under the visible light irradiation ($\lambda > 400$ nm), HM-TiPPh exhibited a remarkable H_2 production rate of 945 μmol·h^{-1}·g^{-1} which is 3.8 times higher than that of TiO_2. Recently the electronic structures of a series of UiO-66-based MOFs based on different metals (Zr, Hf, Th, Ti, U, and Ce) were calculated and only Ce^{4+} promoted the ligand-to-metal charge transfer [195]. In addition, functionalization of the BDC organic linker with various groups was found to fine-tune the band gap of various UiO-66-based MOFs. It would be interesting to synthesize those MOFs and test their performance against prediction. A series of new MOF structures constructed from [Metal–Carbon-(Benzene)$_i$-Chain]$_n$ rings ([M-CB$_i$C]$_n$, M = Ti, V, and Cr, i = 0, 1, 2…, n = 2–6) were calculated to be thermodynamically stable [196]. The optical response to incoming light of [M-CB$_i$C]$_n$ rings could be adjusted to cover the entire visible solar

spectrum range and exhibit red shift by either increasing the edge number n or filling the *d* bands in connecting transition metals. As a new emerging hot topic, single-atom catalysts, as a new class of promising catalysts featuring atomically dispersed metal atoms anchored on supports, greatly improve the utilization of metal active sites and have drawn increasing attention recently. Fang et al. successfully confined single Pt atoms into Al-TCPP, in which electron transfer from the MOF photosensitizer to the Pt acceptor for effective hydrogen production from water under visible light irradiation (Fig. 7c) [197]. The supported single Pt atoms exhibited high activity with a turnover frequency of 35 h^{-1}, about 30 times higher than that of Pt nanoparticles. In addition, MOF-derived nanostructures can also serve as effective catalysts for H_2-producing photocatalyst. A Cd-MOF was subject to doping with Zn^{2+} and Ni^{2+} ions followed by solvothermal sulfidation and thermal annealing to generate $Zn_xCd_{1-x}S$ solid solutions decorated with NiS cocatalyst [198]. By adjusting the doping metal concentration in MOFs, the chemical compositions and bandgaps of the heteroconjugates can be fine-tuned and the optimized NiS/$Zn_{0.5}Cd_{0.5}S$ efficiently catalyzed the hydrogen evolution at a rate of 16.78 $mmol{\cdot}g^{-1}{\cdot}h^{-1}$ under visible-light irradiation. Using thermally stable MOFs as hard templates, Xiao and Jiang incorporated metal nitrates into MOFs to afford metal oxide replica, which could be further converted to metal sulfides via a facile sulfuration process [199]. Significantly, the hierarchically porous CdS obtained using MIL-53(Al) template exhibited excellent hydrogen production performance that was superior to the bulk and nanosized CdS counterparts, manifesting the advantages of the porous nanostructure in photocatalysis.

The water splitting reaction to generate O_2 has been studied less than the H_2 production reaction, likely due to the sluggish 4e transfer process and the poor stability of most MOFs under water oxidation conditions. In 2011, Wang et al. reported MOFs for water oxidation using cerium ammonium nitrate as an oxidant [200]. Three iridium-based water oxidation catalysts, [Cp*Ir^{III}(dcppy)Cl], [Cp*Ir^{III}(dcbpy)Cl]Cl, and [Ir^{III}(dcppy)$_2$-$(H_2O)_2$]OTf, (dcppy = 2-phenylpyridine-5,4′-dicarboxylic acid; dcbpy = 2,2′-bipyridine-5,5′-dicarboxylic acid) were incorporated into the framework of UiO-67 and exhibit good turnover frequencies of up to 4.8 h^{-1}. They later constructed two highly stable MOFs using elongated dicarboxylate bridging ligands derived from Cp*Ir(L)Cl complexes (L = dibenzoate-substituted 2,2′-bipyridine, bpy-dc, or dibenzoate-substituted 2-phenylpyridine, ppy-dc) and $Zr_6O_4(OH)_4$(carboxylate)$_{12}$ cuboctahedral SBUs as effective water oxidation photocatalysts (Fig. 7d) [201]. Detailed mechanistic studies were carried out and demonstrate that MOFs are a great platform to study catalytic mechanisms of molecular species by taking advantage of site isolation in MOF structures and the ease of isolating solid materials from reaction mixtures for further spectroscopic and other characterizations. Nepal and Das incorporated the water oxidation catalyst $Mn^{III}(\mu\text{-}O)_2Mn^{IV}$ into the water-stable MIL-101(Cr) and the resulting composite exhibited much enhanced stability compared to the homogeneous catalyst, owing to the prevention of undesired intermolecular interaction between MnTD molecules [202]. Compared to the rare and expensive noble metals, iron is an abundant cheap metal that is suitable for catalyst development. Chi et al. investigated a series of iron-containing MOFs, MIL-53(Fe), MIL-88B(Fe), and MIL-101(Fe) for photocatalytic water oxidation [203]. In the presence of $[Ru(bpy)_3]^{2+}$ as the photosensitizer, MIL-101(Fe) showed superior catalytic performance (turnover frequency (TOF) = 0.10 s^{-1}) to that of other reported Fe-based catalysts. The sandwich-type polyoxometalate (POM) $[(PW_9O_{34})_2Co_4(H_2O)_2]^{10-}$ was immobilized in the hexagonal channels of the Zr^{4+} porphyrinic MOF-545 as a catalyst for water oxidation [204]. It exhibited a high photocatalytic activity (TOF = 40×10^{-3} s^{-1}) and good stability for visible-light-driven water oxidation. In addition to the investigation on the half reactions for water splitting, an aluminum-based MOF constructed from 2-aminoterephthalate (ATA) and further impregnated with Ni^{2+} ions was reported to generate a photocatalyst for overall water splitting [205]. The Ni^{2+} cation coordinated to the amino group of ATA^{2-} acted as the H_2 evolution site and the benzene ring of the ligand enhanced O_2 generation. It was postulated that the close proximity of both H_2 and O_2 production sites was responsible for the unusual whole water splitting activity.

Another field that MOF catalysts have demonstrated unique advantages is the reduction of carbon dioxide to generate value-added organic products. MOFs are known to be among the best-performing absorbents CO_2 capture, which would be a great advantage to support well-designed catalytic systems. NH_2-MIL-125(Ti) is the first reported MOF catalyst for CO_2 reduction to formate ($HCOO^-$) under visible light irradiation (Fig. 7e) [206]. Since then various MOF catalysts have been developed with enhanced activity. The porphyrin-based PCN-222 was found to selectively capture and further photoreduce CO_2 to formate with high efficiency (3.0 $\mu mol{\cdot}h^{-1}$) [207]. The presence of a deep electron trap state in PCN-222 effectively inhibited the electron-hole recombination and resulted in high catalytic activity. Zhang et al. incorporated coordinatively unsaturated Co sites into the porphyrin units of MOF-525 to generate MOF-525-Co, which showed significantly enhanced photocatalytic conversion of CO_2 compared to the parent MOF [208]. In another related work, Chen et al. tested a series of zirconium polyphenolate-decorated-(metallo)porphyrin MOFs ZrPP-*n* for their ability to photoreduce CO_2 [209]. The phenolic ligands were different from other more common carboxylate ligands, and the MOFs exhibited excellent stability against harsh conditions from moderately acidic (pH = 1) to strongly basic (20 M NaOH). ZrPP-1-Co exhibited not only high CO_2 trapping capability but also high photocatalytic activity for reducing CO_2 into CO ($\sim$14 $mmol{\cdot}g^{-1}{\cdot}h^{-1}$) under visible-light irradiation. In practical situations like flue gas cleaning, CO_2 is only present in low partial pressure and it is ideal for a photocatalyst to be able to enrich CO_2 and further catalyze its reduction. Kajiwara et al. investigated the UiO-67-based Zr-bpdc/RuCO (bpdc = biphenyl-4,4′-dicarboxylate) bearing the Ru^{II}–CO complex active for CO_2 reduction [210]. The catalyst presented comparable CO_2 reduction activities with the corresponding homogeneous Ru^{II} catalyst. More importantly, the PCP-Ru^{II} displayed almost identical catalytic activity even at very low CO_2 concentrations (5% CO_2/Ar), highlighting the synergistic effect between the CO_2 adsorption and catalytically active sites within the PCP-Ru^{II} composite (Fig. 7f). Wang et al. studied a series of cobalt-based MOFs possessing different coordination environments and determined that the neighboring μ-OH^- ligands were crucial for high catalytic activity for CO_2

reduction [211]. The μ-OH^- ligands can cooperate with the Co centers by acting as both hydrogen-bonding donors and local proton sources to improve the performance of photocatalytic CO_2 reduction.

Electrocatalytic reactions

As promising non-noble metal electrocatalysts for oxygen reduction reaction (ORR), oxygen evolution reaction (OER), hydrogen evolution reaction (HER), and carbon dioxide reduction, MOFs exhibit superior properties including large surface area, tunable pore size and channels, designable structures, and homogeneous dispersion of open active centers [212]. However, MOFs are usually restricted by their poor conductivity and especially instability in electrochemical systems. In most early studies within this area, MOFs have served as sacrificial templates to afford various nanostructured materials with both high conductivity and stability, such as porous carbons, metal oxides, metal (oxides)/carbon composites, and other metal-containing compounds [213,214]. Inherited with the advantages of pure MOFs to a certain degree, including high surface area, tailorable porosity, and easy functionalization with other heteroatoms or metal/metal oxides, MOF derivatives not only greatly extend the catalytic application, but also avoid some major drawbacks of pristine MOFs.

The ORR at the cathode of a proton exchange membrane fuel cell (PEMFC) is an important electrocatalytic reaction. Platinum group metals (PGMs) are currently the catalyst materials of choice for this reaction, but their high cost and limited reserves prevent the large-scale commercial utilization of PEMFCs. MOF derivatives have shown great potentials as promising alternative non-PGM ORR catalysts. Ma et al. heated a cobalt imidazolate MOF at 750 °C and the resulting material demonstrates ORR activity with an onset potential of 0.83 V [215]. Chen et al. treated a series of bimetallic ZIFs based on ZIF-8 and ZIF-67 with varied ratios of Zn/Co at 900 °C for 2 h under a nitrogen atmosphere to generate porous carbon with large surface area, high graphitization degree, and highly dispersed N and CoNx active species [216]. Upon additional P doping, the ORR activity of P-CNCo-20 surpassed those of Pt/C catalyst and most other non-precious metal materials. Shang et al. synthesized a hierarchically porous Co,N co-doped carbon nanoframework (Co,N-CNF) using a Zn,Co zeolitic imidazolate framework (Zn,Co-ZIF) precursor and a mesoporous silica protected calcination strategy [217]. The material possessed superior ORR catalytic activity to Pt/C at the same loading in alkaline media and comparable to Pt/C in acidic media. Zhu et al. developed honeycomb-like porous carbon nanostructures from MIL-101-NH_2 encapsulated with thiourea and cobalt chloride [218]. The resulting Co_9S_8@CNS900 exhibited comparable ORR catalytic activity to that of Pt/C under alkaline conditions. Jiao et al. used a mixed-ligand strategy to incorporate iron into the porphyrinic MOF PCN-222, and the subsequent pyrolysis generated high-content (1.76 wt%) single-atom iron-implanted N-doped porous carbon (Fe_{SA}-N-C) with excellent ORR activity surpassing other non-noble-metal catalysts and Pt/C in both alkaline and acidic media (Fig. 8a) [219]. A combination of highly active Fe sites, hierarchically porous structure with oriented mesopores, and high conductivity were responsible for the high ORR catalytic performance.

Electrocatalytic water splitting, which combines HER and OER, is one of the most promising ways for clean energy conversion and utilization. Jiao et al. used pyrolysis and phosphating processes to turn sandwich-type MOF/graphene oxide into layered CoP/reduced graphene oxide (rGO) composite, which exhibited good bifunctional HER and OER activities in basic solution [220]. Ma et al. prepared hybrid porous nanowire arrays composed of strongly interacting Co_3O_4 and carbon through carbonization of a Co-naphthalenedicarboxylate MOF grown on Cu foil [221] (Fig. 8b). The electrode exhibited a low onset potential of 1.47 V vs RHE (reversible hydrogen electrode) and a stable current density at 1.52 V in 0.1 M KOH solution. Wu et al. pyrolyzed a HKUST-1-based MOF, $[Cu_2(BTC)_{4/3}(H_2O)_2]_6[H_3PMo_{12}O_{40}]$ (NENU-5), to generate metal carbide nanocrystallites MoC_x without coalescence and excess growth (Fig. 8c) [222]. The uniform and highly mesoporous structure of MoC_x enabled remarkable electrocatalytic activity for HER in both acidic and basic solutions with good stability. Cai et al. developed a strategy for the synthesis of metal oxide@MOF or metal hydroxide@MOF hybrid arrays on various substrates using metal oxide and hydroxide nanostructured arrays as self-sacrificing templates [223]. Subsequent pyrolysis yielded metal oxide@MOF-derived porous carbon hybrid arrays with well-aligned hierarchical structure, which can be used directly as an efficient electrode for both HER and OER and exhibited higher activity than the corresponding counterparts did.

Electroreduction of CO_2 is a desirable process to turn this greenhouse gas into value-added chemical products. Zhao et al. developed a ZIF-8 assisted strategy to generate Ni single atoms distributed in nitrogen-doped porous carbon (Ni SAs/N-C) for active CO_2 reduction (Fig. 8d) [224]. The TOF reached 5273 h^{-1} and the selectivity to CO production was over 71.9% at 0.89 V. Using ZIF-8 as the MOF precursor and doped ammonium ferric citrate as the iron source, Ye et al. prepared isolated Fe-nitrogen sites within carbon matrix as efficient catalyst for both ORR and the CO_2 electroreduction reaction [225]. Pan et al. prepared nitrogen-coordinated Fe or Co sites atomically dispersed into carbons (M-N-C) containing bulk- and edge-hosted M-N_4 coordination through pyrolysis of the corresponding metal-doped ZIF-8 MOFs [226]. Fe was found to be more active than Co in M-N_4 for electroreduction of CO_2 into CO with a higher CO Faradaic efficiency (FE) (93% vs. 45%).

Electrochemical reduction of N_2, another newly emerging frontier, can also be efficiently promoted by MOF-based materials. Mukherjee et al. reported a nitrogen-doped carbon catalyst derived from ZIF-8 via one-step pyrolysis, which exhibited a remarkable reduction rate of NH_3 with a Faradaic efficiency (FE) up to 10.2% at −0.3 V vs. RHE [227]. Guo et al. synthesized CoP hollow nanocages (CoP HNC) with highly exposed surface active sites and hierarchical structure from ZIF-67. When applied for N_2 reduction, CoP HNC exhibited high FE (7.36%) at 0 V vs RHE [228]. By the pyrolysis of Ru(acac)$_3$@ZIF-8 composite, single-atom Ru catalyst was recently reported for N_2 reduction for the first time, achieving a record high Faradaic efficiency of 29.6% for NH_3 production [229]. These investigations provide new insights into the rational design of efficient N_2 reduction catalysts based on MOFs.

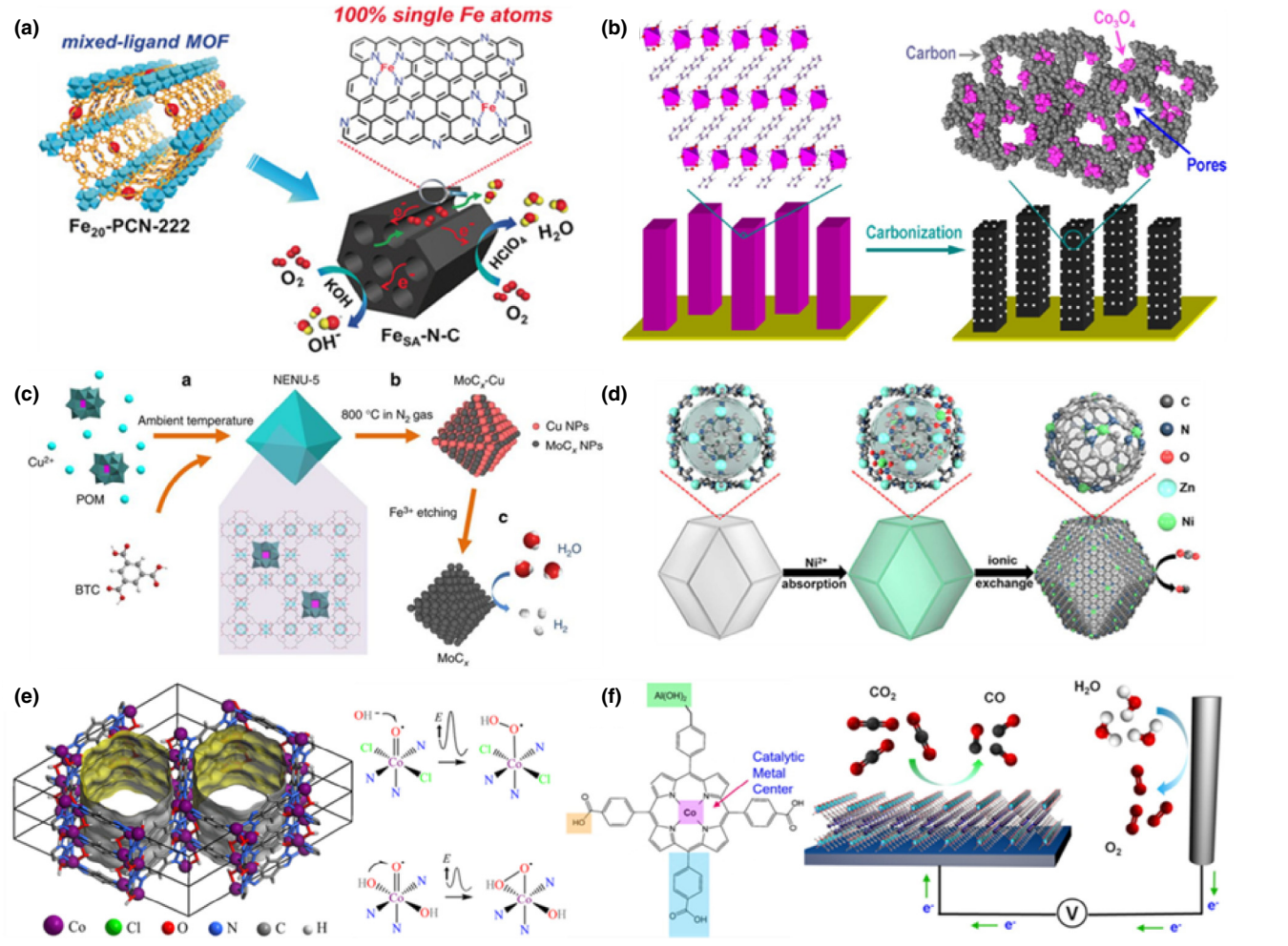

FIGURE 8

(a) Illustration of the mixed-ligand strategy for the construction of single-atom Fe implanted N-doped carbon for efficient ORR [219]. Reproduced with permission from Ref. [219]. Copyright 2018, Wiley-VCH. (b) Schematic illustration showing the fabrication of Co_3O_4-C nanowire arrays for OER [221]. Reproduced with permission from Ref. [221]. Copyright 2014, American Chemical Society. (c) The synthetic procedure for porous MoC_x nano-octahedrons by a MOF-assisted strategy [222]. Reproduced with permission from Ref. [222]. Copyright 2015, Nature Publishing Group. (d) Scheme for the construction of Ni SAs/N-C [224]. Reproduced with permission from Ref. [224]. Copyright 2017, American Chemical Society. (e) Postsynthetic ion exchange of MAF-X27-Cl to construct MAF-X27-OH for highly efficient OER [53]. Reproduced with permission from Ref. [53]. Copyright 2016, American Chemical Society. (f) The cobalt-porphyrin MOF, $Al_2(OH)_2TCPP$-Co, as electrocatalyst for CO_2 reduction [241]. Adapted with permission from Ref. [241]. Copyright 2015, American Chemical Society.

In very recent years, MOFs have also been directly used as electrocatalysts with a number of distinctive advantages. The highly ordered structure of MOFs allows the precise design and control of the active sites as well as understanding of the reaction mechanism. The high porosity and surface compared to other porous materials will aid in the exposure of active sites and boost the efficiency of the reaction. Still there are major challenges especially in terms of stability. Electrocatalytic reactions are often performed under strongly acidic or basics conditions in which not many MOFs can survive. Another challenge comes from the structure of MOFs with low electric conductivity. Utilization of special ligands and combination of MOFs with more conductive materials are the most common strategies to address the challenges. Jahan et al. used pyridine-functionalized graphene as a template to construct a composite material containing a porphyrin-based iron MOF [230]. The composite shows much higher selectivity for ORR due to the synergistic effect between the reduced graphene oxide, pyridinium linker, and the porphyrin catalytic center. Lu et al. performed postsynthetic ion exchange on $[Co_2(\mu\text{-Cl})_2(btta)]$ (MAF-X27-Cl, H_2bbta = 1*H*,5*H*-benzo(1,2-d:4,5-*d*′)bistriazole) to generate $[Co_2(\mu\text{-OH})_2(bbta)]$ (MAFX27-OH) which contained both open metal sites and hydroxide ligands (Fig. 8e) [53]. The catalyst showed excellent stability under strongly basic conditions and good electrocatalytic activities for OER with an overpotential of 292 mV at 10.0 $mA{\cdot}cm^{-2}$ in 1.0 M KOH solution. The same research group recently developed a two-step, single-crystal to single-crystal, postsynthetic modification approach to generate $[Fe_3(\mu_3\text{-O})(bdc)_3]_4[Co_2(na)_4(L^T)_2]_3$ [231]. The MOF contained a dicobalt cluster and showed good electrocatalytic activities for OER with an overpotential of 225 mV at 10 $mA{\cdot}cm^{-2}$ at pH 13. Zhao et al. developed ultrathin Ni-Co mixed metal MOF nanosheets

on glassy-carbon electrodes for OER (overpotential = 250 mV at 10.0 mA·cm^{-2} in 1 M KOH solution) [232]. Both the open metal sites and the coupling effect between Ni and Co were crucial for tuning the electrocatalytic activity. Another 2D Ni-MOF comprising nickel ions and BDCs was also fabricated by Zhu et al. Thanks to the high density of active sites and high oxidation states of nickel species, the ultrathin Ni-MOF electrocatalysts exhibited remarkable activity, favorable kinetics, and strong durability for urea oxidation reaction (UOR) [233]. Duan et al. also developed a mixed metal Ni-Fe MOF system for OER [234]. The MOF was grown in a one-pot fashion from nickel acetate, iron(III) nitrate, and 2,6-naphthalenedicarboxylic acid in the presence of nickel foam as substrate. The resulting ultrathin nanosheet arrays of 2D MOFs demonstrated good activity for OER (overpotential of 240 mV at 10.0 mA·cm^{-2} in 0.1 M KOH solution). Wen et al. reported an alkaline-stable anionic boron imidazolate framework, named BIF-89, featuring uncoordinated carboxylate groups which can effectively capture Fe(III) ions. The resulting Fe@BIF-89 showed high OER performance under alkaline condition surpassing that of the benchmark IrO_2/C catalyst [235]. While most OER reactions involving MOF catalysts have been achieved under basic conditions, neutral pH conditions are more benign and attractive. Mukhopadhyay et al. incorporated the Keggin anion $[CoW_{12}O_{40}]^{6-}$ into ZIF-8, and the composite catalyst showed good OER activity with a TOF of 10.8 mol O_2·(mol Co)$^{-1}$·s^{-1} and recyclability up to 1000 catalytic cycles under neutral conditions [236]. Up until now, most literatures on MOFs for OER assumed that the chemical structures of MOFs could be maintained under electrochemical conditions. Very recently, Su et al. found that NiFe Prussian blue analogues (PBA) can be transformed into amorphous nickel hydroxide after the electrochemical treatment [237]. Using operando X-ray spectroscopic studies, they found that the in-situ generated $Ni(OH)_2$ could then create $NiOOH_{2-x}$ under applied potential which improved the OER performance. Future studies in this field must also address the intrinsic reaction mechanism during OER process to help researchers construct correct structure–property relationships.

As the other half reaction of water splitting, HER using MOF electrocatalysts has also been investigated. Qin et al. synthesized two POM-based MOFs, $[TBA]_3[\varepsilon\text{-}PMo_8^{V}Mo_4^{VI}O_{36}(OH)_4Zn_4][BTB]_{4/3}$·xGuest (NENU-500, BTB = benzene tribenzoate, TBA^+ = tetrabutylammonium ion) and $[TBA]_3[\varepsilon\text{-}PMo_8^{V}Mo_4^{VI}O_{37}(OH)_3Zn_4][BPT]$ (NENU-501, BPT = [1,1′-biphenyl]-3,4′,5-tricarboxylate) as efficient electrocatalysts for HER [238]. The combination of the redox activity of the POM unit and the porosity of MOFs resulted in good HER activity and NENU-500 exhibited an overpotential of 237 mV at 10 mA·cm^{-2}. Wu et al. found that two polymorphic Co-MOFs (CTGU-5 and -6) can be selectively crystallized into the pure 2D or 3D net using an anionic or neutral surfactant, respectively [239]. The 2D CTGU-5 contained coordinated water in its structure, which can provide more open access to reactants. After integration of the cocatalyst acetylene black (AB), AB&CTGU-5 (1:4) showed good HER catalytic activity of a low onset potential of 18 mV and long-term stability.

Carbon dioxide reduction is a useful and valuable way for carbon mitigation. However, it is an energetically and kinetically challenging process. The one-electron reduction of CO_2 to $CO_2^{\cdot-}$ has a very high potential of −2 V versus the normal hydrogen electrode (NHE), and catalytic reduction of CO_2 often results in multiple products including carbon monoxide, formic acid, formaldehyde, methanol, and methane. MOF-based electrocatalysts have been shown to be effective at alleviating some of these challenges. Hod et al. installed the catalyst Fe-TPP into Fe porphyrin-based MOF-525 and deposited the material onto electrode surfaces, generating a mixture of CO and H_2 as products in 1 M $TBAPF_6$ acetonitrile electrolyte solution [240]. Kornienko et al. synthesized thin films of a cobalt-porphyrin MOF, $Al_2(OH)_2$TCPP-Co as an efficient electrocatalyst that selectively reduced carbon dioxide to carbon monoxide in aqueous electrolytes (Fig. 8f) [241]. The selectivity for CO production in over 76% and the catalyst is stable after 7 h with a per-site turnover number (TON) of 1400. In situ spectroelectrochemical measurements revealed that Co(I) reduced from Co(II) was the majority of catalytic centers in this MOF.

Chemical sensors

The highly ordered and tunable structures of MOFs make them a great platform for constructing chemical sensors. Inclusion of a guest molecule often results in the change of luminescence for the MOF hosts. Many diverse chemical functionalities have been incorporated into the coordination nanospace of MOF materials and shown sensing applications for biomolecules, metal ions, explosives, environmental toxins, and others [242–247]. Nagarkar et al. synthesized the fluorescent MOF $[Cd(NDC)_{0.5}(PCA)]$ (NDC = 2,6-napthalenedicarboxylic acid, PCA = 4-pyridinecaboxylic acid) from the luminescent NDC and PCA ligands and demonstrated its usage as a highly selective detector for the nitro explosive 2,4,6-trinitrophenol (TNP) in the presence of other very similar nitro aromatics in both aqueous and organic solutions (Fig. 9a) [248]. The selectivity resulted from a combination of electron and energy transfer mechanisms as well as electrostatic interactions between TNP and the fluorophore. Zhang et al. tested the detection of DNA with the amine-functionalized UiO-66-NH_2 [249]. While the sensing system can distinguish complementary and mismatched DNA sequences down to single base mismatch with high selectivity and good reproducibility, the related UiO-66 showed no activity. The hydrogen bond interaction between the single-stranded DNA (ssDNA) and the amino group of UiO-66-NH_2 was assumed to be crucial for the detection to work. Jiang et al. prepared zirconium-porphyrin framework PCN-225 and found this MOF to change its fluorescent intensity with varying pH, of which the range of pH 7 to 10 is the most sensitive range for intensity response [250]. Zhan et al. used ZnO nanorods to serve not only as the template but also the source to provide Zn^{2+} ions for the formation of ZIF-8, and the resulting ZnO@ZIF-8 nanorods showed selective photoelectrochemical response for hydrogen peroxide in serous buffer solution [251]. The core–shell structure of this MOF material was crucial for the H_2O_2 detection. Some of the main organic pollutants in wastewater include organic explosives and antibiotics, which are in trace amounts and therefore are hard to detect. Wang et al. synthesized the isostructural Zr (IV)-based MOFs $Zr_6O_4(OH)_8(H_2O)_4(CTTA)_{8/3}$ (BUT-12, H_3-CTTA = 5′-(4-carboxyphenyl)-2′,4′,6′-trimethyl-[1,1′:3′,1″-terphenyl]-4,4″-dicarboxylic acid) and $Zr_6O_4(OH)_8(H_2O)_4(TTNA)_{8/3}$

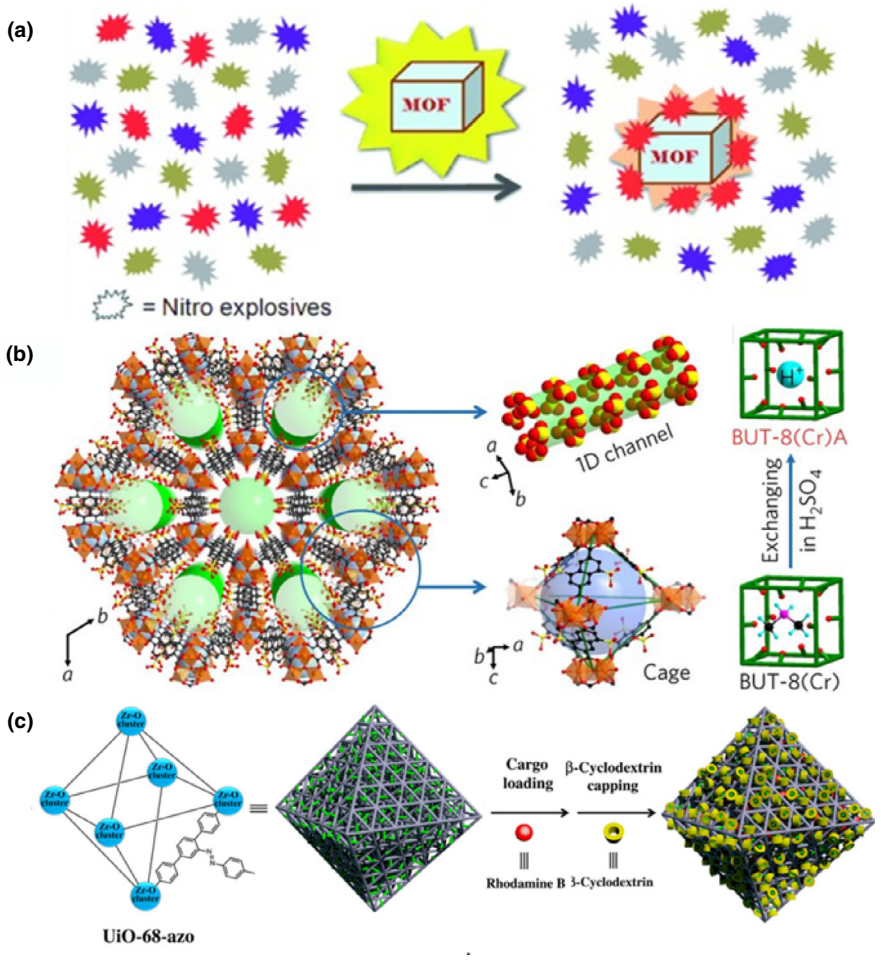

FIGURE 9

(a) MOF-based sensor for the selective detection of target nitro explosives in the presence of other nitro compounds [248]. Reproduced with permission from Ref. [248]. Copyright 2013, Wiley-VCH. (b) The crystal structure of BUT-8(M) and schematic illustration of the ion exchange in BUT-8(Cr) to form BUT-8(Cr)A [254]. Reproduced with permission from Ref. [254]. Copyright 2017, Nature publication group. (c) Schematic illustration of the synthesis of UiO-68-azo and further construction of RhB-loaded, β-CD–capped UiO-68-azo with azobenzene units as stalks encircled by β-CD on the surface [267]. Adapted with permission from Ref. [267]. Copyright 2016, American Association for the Advancement of Science.

(BUT-13, H_3TTNA = 6,6′,6″-(2,4,6-trimethylbenzene-1,3,5-triyl) tris(2-naphthoic acid)) which were highly fluorescent and water stable [252]. The fluorescence of these MOFs was efficiently quenched by trace amount (down to ppb levels) of nitrofurazone (NZF) and nitrofurantoin (NFT) antibiotics as well as 2,4,6-trinitrophenol (TNP) and 4-nitrophenol (4-NP) organic explosives in aqueous solution. It was interesting to note that these MOFs achieved the simultaneous selective detection and removal of specific antibiotics and organic explosives from water, thus they were useful in both monitoring water quality and treating waste water.

Proton conductivity

Proton conducting materials are essential for fuel cells as they serve as the electrolytes. Application of MOFs for proton conduction has been a rather nascent field but significant progress has already been made [253]. The crystallinity, chemically functionalizable pores, high surface area, and tunability give MOFs unique advantages as proton-conductive materials. One common problem of many proton-conductive MOFs is their good conductivity at high relative humidity (RH), but significantly decreased conductivity at reduced RH. Yang et al. synthesized a chemically stable and structurally flexible Cr^{3+}-based MOF $Cr_3(\mu_3\text{-}O)(H_2O)_3(NDC(SO_3H_{5/6})_2)_3$ (BUT-8(Cr)A, $NDC(SO_3H)_2^{2-}$ = 4,8-disulfonaphthalene-2,6-dicarboxylate) which exhibits high proton conductivity up to 1.27×10^{-1} S·cm^{-1}at 100% RH and 80 °C [254]. The MOF had one-dimensional channels with high density sulfonic acid (–SO_3H) sites on channel surfaces, and it showed remarkable stability in 10 M sulfuric acid or concentrated hydrochloric acid for one week (Fig. 9b). The flexible framework together with its sulfonic acid allow BUT-8(Cr)A to self-adapt under different humid conditions to ensure smooth proton conduction mediated by water molecules. Nagarkar et al. constructed the oxalate (ox)-based MOF $[(Me_2NH_2)_3(SO_4)]_2[Zn_2(ox)_3]$ which exhibited good proton conductivity under both anhydrous conditions (1×10^{-4} S·cm^{-1} at 150 °C) and wet conditions (4.2×10^{-2} S·cm^{-1} at 98% RH and 25 °C [255]. The MOF's water-assisted proton conductivity under wet conditions was comparable to that of Nafion, an organic polymer currently used for practical fuel cell applications. Zhang et al.

recently studied the effect of imidazole arrangements on proton conductivity in MOFs [256]. An Fe-MOF as the blank, an imidazole@Fe-MOF (Im@Fe-MOF) with physically adsorbed imidazole molecules, and an imidazole-Fe-MOF (Im-Fe-MOF) with imidazole molecules coordinated with the metal centers were synthesized and compared side by side with regard to their proton conductivity properties. It was found that the proton conductivity of Im-Fe-MOF (1.21×10^{-2} S·cm^{-1}at 60 °C and 98% RH) is about two orders of magnitude greater than those of Fe-MOF and Im@Fe-MOF. The study concludes that imidazole molecules fixed by coordination bonds in the MOF are much more prone to conduct protons than imidazole molecules disorderly present in MOF pores do. This effect, however, appears to be dependent on the particular MOF system that was used. Ye et al. incorporated imidazole molecules into the porous pristine MOF NENU-3 through direct one-step evaporation to generate Im@(NENU-3) ($[Cu_{12}(BTC)_8(H_2O)_{12}][HPW_{12}O_{40}]\cdot[(CH_3)_4N]_2\cdot 9H_2O\cdot 14.5Im$) in which the terminal metal sites were still coordinated with water molecules while the free imidazole molecules filled the inside pore spaces of the MOF [257]. By following a different two-step imidazole incorporation strategy [258], the researchers also prepared Im-Cu@(NENU-3a) ($[Cu_{12}(BTC)_8(Im)_{12}][HPW_{12}O_{40}]\cdot[(CH_3)_4N]_2\cdot 8H_2O\cdot 0.25Im$) in which imidazole molecules coordinated with the Cu sites. The proton conductivity of Im@(NENU-3) (1.82×10^{-2} S·cm^{-1} at 70 °C and 90% RH) was about two orders of magnitude greater than that of Im-Cu@(NENU-3a) (3.16×10^{-4} S·cm^{-1} at 70 °C and 90% RH) and slightly higher than that of Im-Fe-MOF (1.21×10^{-2} S·cm^{-1}at 60 °C and 98% RH). It was postulated that two proton-transfer mechanisms are present in Im@(NENU-3), namely, (i) the Grotthuss (hopping) mechanism from the hydrogen bond network made of free imidazole and water molecules and (ii) the vehicular mechanism in which free water molecules serve as carriers and carry protons through self-diffusion. These works illustrate that the similar or same strategy to improve proton conductivity may not work for different MOFs due to structural variation, again confirming the idea that the structure of a MOF determines its function.

Biomedicine

In recent years, MOFs have also found applications in biomedicine. Nanoscale MOFs have advantages including rich structural diversity, high loading capacity, and biodegradability over other conventional nanomedicines. Emerging applications of MOFs in this field include protection and delivery of molecular therapeutics, gasotransmitter gases, and biopharmaceuticals, biosensing, biocatalysis, biobanking, and cell and virus manipulation [259–262].

Benefitting from exceptionally ultrahigh surface areas with large pore sizes, MOFs can be extensively used for the delivery and controlled release of therapeutic compounds in the last decade. In 2006, Horcajada et al. demonstrated the remarkable capacity for drug hosting and controlled delivery of porous MOFs for the first time [263]. Thanks to their mesoporosity, MIL-100 and MIL-101 can realize high ibuprofen encapsulation up to 60%. A porous anionic metal–organic framework, bio-MOF-1, constructed using adenine as a bimolecular building block was employed by An et al. for the storage and release of procainamide HCl, an important cationic antiarrhythmic drug [264]. This is the first example of cation-triggered drug release based on MOFs. Similarly, via the oxidation of neutral MOF-74-Fe(II), Hu et al. developed a cationic drug carrier, MOF-74-Fe(III) [265]. The cationic MOF-74-Fe(III) presented a loading capacity around 15.9 wt% for ibuprofen anions with controllable release, making it a promising drug delivery host. Rieter et al. developed a general strategy to formulate highly degradable nanoparticles based on Pt-containing nanoscale coordination polymers with the formula of $Tb_2(DSCP)_3(H2O)_{12}$ (where DSCP represents disuccinatocisplatin) and realized the effective delivery of 46.7% Pt-based drugs to cancer cells [266]. Recently, Meng et al. reported a dual stimuli-responsive MOF by tethering β-CD on the surface of UiO-68-azobenzene (β-CD–capped UiO-68-azo) through supramolecular complexation (Fig. 9c) [267]. Azobenzene groups provided photo-controllable *cis*/*trans* isomerization and the isomerization of azobenzene from *trans* to *cis* promoted the dethreading of the gating β-CD to regulate cargo release.

Although the investigations on biomedicine applications are still in their infancy, MOFs have presented great potentials and unique advantages. With continued endeavors, we believe more studies on MOFs as drug deliverers will be targeted in the future.

Emerging related research and trends

Multivariate MOFs

Multivariate (MTV) MOFs are a class of MOFs containing multiple functionalities such as different metal ions and linkers. The deliberate introduction of heterogeneity into the highly ordered MOF structures often result in superior functional performance than the simple linear combination of pure constituents [268]. The concept of the MTV MOFs was first proposed and realized by Yaghi and coworkers in 2010 with the synthesis of eighteen MTV MOF-5 type structures that contain up to eight distinct functionalities in one phase [269]. As a demonstration for the power of this approach, MTV-MOF-5-EHI exhibited up to 400% better selectivity for carbon dioxide over carbon monoxide compared with its best same-link counterparts. One significant challenge with MTV MOFs is the difficulty with structural characterization of the intermingling functional groups with the MOFs, i.e., whether these groups are present as random, alternating, or various cluster forms. To address this challenge, Kong et al. developed a methodology combining rotational echo double-resonance (REDOR) solid-state nuclear magnetic resonance (NMR) technique with molecular simulations and demonstrated its effectiveness of predicting and validating both the structures and functions of MTV MOFs [270]. The method can be applied to the general problem of spatial disorder in ordered materials. Sun et al. developed a facile one-pot method to incorporate multi-functionalities into stable Zr-MOFs through mixing ligands of different geometry and connectivity [271]. A series of tetratopic TCPP ligands were successfully integrated into UiO-66 while maintaining the crystal structure, morphology, and stability of the MOF. A total of 49 MTV MOFs were prepared through a combination of H_2BDC derivatives and TCPP ligands, out of which MOFs modified with FeTCPPCl were demonstrated to preserve the catalytic activity of the ligand. Dong et al. achieved programmable controlled release of ibuprofen, rho-

damine B, and doxorubicin with MIL-101-based MTV MOFs (Fig. 10a) [272]. The controlled drug release cannot be achieved with the physical mixture of the single component MOF counterparts, demonstrating the unique advantage of MTV MOFs.

Defective MOFs

Introduction of defects into the structure of MOFs is another way to introduce structural heterogeneity. Such defects in MOFs can provide new functional sites, which are otherwise non-existent in the parent MOFs to enhance gas adsorption and separation, boost catalytic activity, and improve electrical and conductive properties [273–275]. A series of studies have been performed on UiO-66, a Zr-based MOF known for its high thermal, chemical, and mechanical stabilities [26]. Wu et al. used acetic acid as the modulator for the synthesis of UiO-66 and demonstrated for the first time that a significant amount of missing-linker defects (up to 10%) is present in the structure of this MOF [276]. The linker vacancies can be systematically tuned by varying the concentration of acetic acid as well as reaction time, and the resulting defective UiO-66 showed a dramatic increase in pore volume (up to 150%), surface area (up to 60%), and CO_2 adsorption ability due to the presence of Zr-coordinated hydroxide groups. Using different modulators trifluoroacetic acid (TFA) and HCl, almost simultaneously, Vermoortele et al. synthesized defective UiO-66 through post-synthetic removal of TFA and thermal dihydroxylation (Fig. 10b) [277]. The UiO-66 prepared this way had a more open structure with additional open metal sites and turned out to be a good catalyst for the Meerwein reduction of 4-*tert*-butylcyclohexanone with isopropanol. Careful examination of the reaction conditions for MOF synthesis can also lead to non-defective "ideal" MOFs. By setting the ligand/metal ratio at 2:1 BDC:Zr and increasing reaction temperature to 220 °C, Shearer et al. prepared "ideal" UiO-66 with unsurpassed thermal stability at up to 450 °C [278]. With extensive usage of X ray diffraction on judiciously prepared UiO-66 single crystals, Trickett et al. elucidated the structural details of the defects in UiO-66 with molecular level precision [279]. Water molecules were found to replace the BDC ligand to create the defects, and charge neutrality was maintained by hydroxide ions. DeStefano et al. also studied the temperature effect during UiO-66 synthesis and achieved for the first time room temperature solution-based synthesis of UiO-66 [280]. This study confirmed other reports that increased reaction temperature results in fewer defects. A maximal number of defect sites (1.3 missing linkers per $Zr_6O_4(OH)_4(bdc)_6$) is generated at a reaction temperature of 45 °C. Cai and Jiang developed a versatile modulator-induced defect-formation strategy using monocarboxylic acid as a modulator and an insufficient amount of organic ligand to generate hierarchically porous MOFs [74]. Mesoporous UiO-66 incorporated with phosphotungstic acid with high stability and reduced transport limit turns out to be a great catalyst for the methanolysis of styrene oxide. Other defective MOFs have also been investigated and the modulator approach is generally applicable. For example, Jiang et al. used TFA to generate the defect-containing USTC-253-TFA with exposed metal centers, which had increased CO_2 uptake (167 %), CO_2/N_2 selectivity, and improved catalytic activity and recyclability in the cycloaddition of CO_2 and epoxide at room temperature, compared to the pristine USTC-253 (Al(OH)(Sbpdc), Sbpdc = 4,4′-dibenzoic acid-2,2′-sulfone) [281].

2D MOFs

Various MOFs can be constructed into 2D nanosheets with active sites exposed on surface rather than in pores and channels, and such 2D MOFs, also termed 2D MOLs (metal–organic layers), often exhibit improved performance in surface-active separation, sensing, catalysis, and other applications [282]. By means of ultrasonication, Li et al. fabricated MOF nanosheets from bulk crystals of a layered MOF, $[Zn(TPA)(H_2O)\cdot DMF]_n$ (MOF-2) [283]. By solvent-assisted interaction, a laminar MOF $[Cu(\mu\text{-}pym_2S_2)(\mu\text{-}Cl)]_n\cdot nY$ (where Y can be MeOH, H_2O or ½EtOH) can be fully delaminated by simple immersion of the crystals in water [284]. Peng et al. developed a soft-physical exfoliation process to construct 1-nm thick molecular sieve nanosheets from the MOF $[Zn_2(bim)_4]_n$ (bim = benzimidazole). The morphological and structural integrity of the MOF can be maintained in the nanosheets with large lateral area and high crystallinity. The 2D MOF exhibited exceptionally high hydrogen gas permeance of up to 2700 gas permeation units (GPUs) as well as high H_2/CO_2 selectivity of 291 [114]. The same research group later developed a modified top-down method to prepared $[Zn_2(bim)_3(OH)(H_2O)]_n$ nanosheets from the layered MOF precursor [285]. The ultrathin MOF membranes of less than 10 nm in thickness demonstrated excellent H_2/CO_2 separation performance with a selectivity of up to 166 and H_2 permeance of up to 8×10^{-7} mol·m^{-2} s^{-1} Pa^{-1} at elevated testing temperatures. Rodenas et al. used a bottom-up approach to synthesize 2D copper 1,4-benzenedicarboxylate (CuBDC) MOF with micrometer lateral dimensions and nanometer thickness [286]. When further incorporated into polyimide matrices to form a composite material, the 2D MOF-polymer composite showed 30–80% higher CO_2/CH_4 selectivity than the polymer membrane alone did, and the selectivity slightly increased with higher CO_2 partial structure, which was opposite to the general observation for both polymeric and conventional MOF-polymer membranes. Tomographic focused-ion-beam scanning electron microscopy indicated a superior occupation of the polymer membrane cross section by the 2D MOF nanosheets but not isotropic crystals. Zhao et al. developed a surfactant-assisted method to prepare a series of 2D M-TCPP (M = Zn, Cu, Cd or Co) nanosheets of less than 10 nm in thickness (Fig. 10c) [287]. The 2D Cu-TCPP nanosheets exhibited the best performance for sensing DNA with a detection limit of 20×10^{-12} M, which was much lower than that of the normal 3D MOF-based particles and comparable to those based on other 2D nanomaterials. In a related work, Wang et al. also synthesized 2D bimetallic MOF nanosheets containing the heme-like ligand TCPP(Fe) (Fe(III) tetrakis(4-carboxyphenyl)porphyrin chloride) [288]. The 2D M-TCPP(Fe) nanosheets can be assembled into multilayer films on electrodes and were capable of detecting H_2O_2, with the GC/$(Co\text{-}TCPP(Fe))_5$ electrode showing a sensitivity of 35.4 μA·cm^{-2}·mM^{-1}, outperforming the natural heme proteins. The fabricated 2D Co-TCPP (Fe) nanosheet-based sensor can be used for the real-time tracking of H_2O_2 secreted by live cells. Huang et al. reported the growth of Au nanoparticles on 2D Cu-TCPP(M) (M = Fe and Co) nanosheets which were used as a sensor to detect glucose

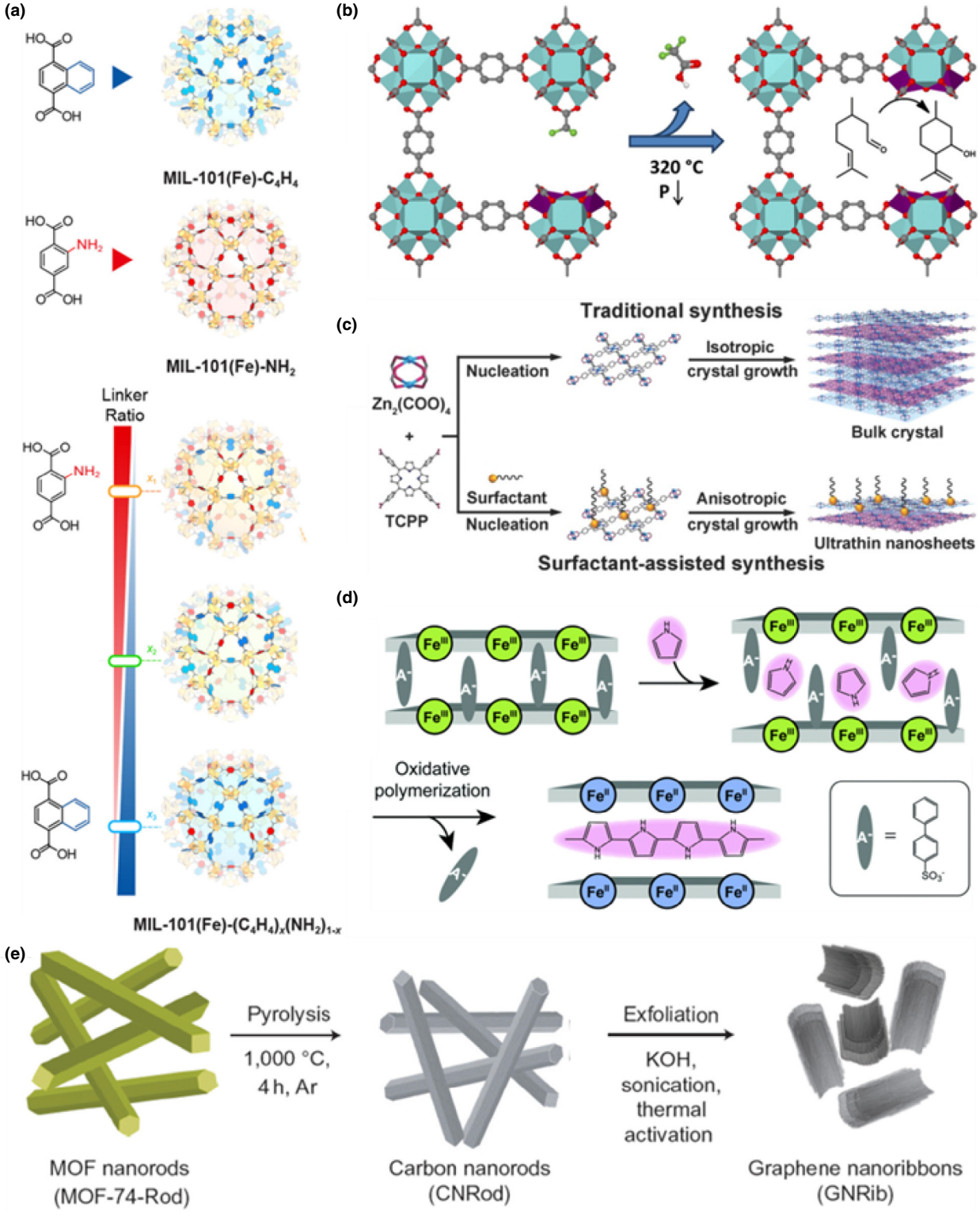

FIGURE 10

(a) Illustration for MTV MOFs with various linker ratios [272]. Reproduced with permission from Ref. [272]. Copyright 2017, American Chemical Society. (b) The use of acetic acid modulator to create defect sites in the well-studied zirconium terephthalate MOF UiO-66 [277]. Reproduced with permission from Ref. [277]. Copyright 2013, American Chemical Society. (c) Illustration for surfactant-assisted synthesis of 2D MOF nanosheets [287]. Reproduced with permission from Ref. [287]. Copyright 2005, Wiley-VCH. (d) Schematic illustration of the intercalation of the Py monomer and the oxidative polymerization of Py by the Fe^{III} ions in the host layers [302]. Adapted with permission from Ref. [302]. Copyright 2008, Wiley-VCH. (e) The thermal transformation of MOF-74-Rod to graphene nanoribbons [322]. Adapted with permission from Ref. [322]. Copyright 2016, Nature publication group.

and a biomimetic catalyst for cascade reactions [289]. Cao et al. used 2D MOF as a precursor for supercapacitor construction [290]. 2D porphyrin paddlewheel framework-3 (PPF-3) MOF nanosheets with a thickness of ca. 12–43 nm were prepared with a surfactant-assisted method and then subjected to simultaneous sulfidation and carbonization to give 2D nanocomposite of $CoS_{1.097}$ nanoparticles and nitrogen-doped carbon (CoSNC). The 2D CoSNC nanocomposite can be used as an electrode material to construct supercapacitor reaching a high specific capacitance of 360.1 $F{\cdot}g^{-1}$ at a current density of 1.5 $A{\cdot}g^{-1}$. The highly ordered structure of related 2D and 3D MOFs made it possible to probe the dimensional dependency of resonance energy transfer. Cao et al. used the donor ligand 4,4′,4″-(benzene-1,3,5-triyl-tris(ethyne-2,1-diyl))tribenzoate (BTE) and the doped acceptor ligand 3,3′,3″-nitro-4,4′,4″-(benzene-1,3,5-triyl-tris(ethyne-2,1-diyl))tribenzoate (BTE-NO_2) with Hf-oxo clusters as the connecting nodes to construct the corresponding 2D and 3D MOFs [291]. Measurement of fluorescence quenching of the donors revealed that energy transfer is more efficient in 3D MOF than in the 2D counterpart, but excitons on the 2D MOF were more accessible to external quenchers than those in the 3D MOF. This work provided mechanistic details on exciton migration in 2D materials involving light-harvesting and fluorescence sensing. 2D MOFs have also found applications in catalysis with the exposed active sites. By modifying the SBUs with monocarboxylic acids such as gluconic acid during 2D MOF synthesis, Shi et al. demonstrated that the hydrophobicity/hydrophilicity around the active sites can be fine-tuned to achieve the photocatalytic oxidation of tetrahydrofuran (THF) to butyrolactone (BTL) with exclusive selectivity over the competing 2-hydroxy tetrahydrofuran product [292]. Through precise control of the solvothermal synthetic conditions, Cao et al. synthesized 2D MOF layers down to single-layer thickness (1.2 ± 0.2 nm) from $[Hf_6O_4(OH)_4(HCO_2)_6]$ SBU and benzene-1,3,5-tribenzoate (BTB) bridging ligand [293]. Further doping with 4′-(4-benzoate)-(2,2′,2″-terpyridine)-5,5″-dicarboxylate (TPY) and coordination with iron centers afforded highly active (up to quantitative conversion and >5000 turnover number) and reusable single-site solid catalysts for the hydrosilylation of terminal olefins. It is interesting to note that the corresponding stacked or interlocked 3D MOFs only result in low (30%)-to-zero conversion, likely due to diffusional constraints for reactants. This work provides one example in which 2D MOF is superior in terms of catalytic activity compared to the 3D MOF counterparts. The major challenges in the synthesis of ultrathin 2D MOF nanosheets are the control of layer thickness and the typically low yield. Ding et al. devised a novel intercalation and chemical exfoliation approach to obtain 2D MOF nanosheets from intrinsically layered 3D MOF crystals [294]. The two-step process started with intercalating the porphyrinic MOF crystals with 4,4′-dipyridyl disulfide through coordination bonding. The following reductive cleavage of disulfide bond with trimethylphosphine resulted in facile exfoliation at room temperature to produce ultrathin (~1 nm) 2D MOF nanosheets in ~57% overall yield. Photooxidation of 1,5-dihydroxynaphthalene to form juglone was studied as a test reaction, and the 2D MOF nanosheets exhibited far superior heterogeneous photocatalytic performance than the 3D MOF counterpart did.

MOF-based composites

The regular pores and channels of various sizes together with the large surface areas of MOFs make them ideal platforms to construct hybrid composite materials [295,296]. The pore space in MOFs provides congenital conditions to introduce functional guests for integrated properties. The controlled integration of MOFs with other functional materials often leads to multifunctional composites with either new properties or collective properties that are superior to the properties of a simple physical mixture of individual components. This is because the multiple functional sites often work synergistically with each other. In addition, the regular channels in MOFs could facilitate mass transport, and the locally confined environment of MOFs could provide stabilization for active species. A large variety of materials have been used to form composites with MOFs, including polymers [297], various active species [298], metal nanoparticles [299,300], enzymes [301], quantum dots, graphene, carbon nanotubes [295], and others. Yanai et al. synthesized a layered 2D MOF $[Ni(dmen)_2]_2[Fe^{III}(CN)_6]]PhBSO_3$ (dmen = 1,1-dimethylethylenediamine; $PhBSO_3^-$ = *p*-phenylbenzenesulfonate) which contains the redox-active $[Fe^{III}(CN)_6]^{3-}$ units [302]. The material shows catalytic activity for the intercalative polymerization of pyrrole (Py) by oxidative polymerization (Fig. 10d). In addition to polymer, Li et al. rationally encapsulated Co(II) complex into the cages of MIL-125-NH_2 to form a Co(II)@MIL-125-NH_2 composite as a photocatalyst [303]. The photoinduced charge can transfer from MIL-125-NH_2 to the Co(II) complex and greatly improves the spatial charge separation, thus significantly boosting the catalytic efficiency for H_2 generation. Metal nanoparticle can also be introduced to construct MOF-based composite to realize the synergetic catalysis. Based on a double solvent approach (DSA) developed by Xu's group, one can realize the complete encapsulation of metal precursors into MOF pores, which guarantees the formation of NPs inside MOFs. For example, ultrafine Pt NPs were exclusively confined into the pores of MIL-101 and showed high activity for ammonia borane dehydrogenation and CO oxidation [304]. In another application, AuNi alloy NPs were immobilized in MIL-101 by DSA and the resultant AuNi@MIL-101 exhibited high hydrogen generation activity for the hydrolysis of ammonia borane [305]. In addition to DSA, Yang et al. reported a Pd nanocubes@ZIF-8 composite material by encapsulation of the Pd nanocubes in ZIF-8 [306]. Making full usage of the synergetic effect between Pd (active sites and photothermal conversion) and ZIF-8 (H_2 enrichment, Pd stabilization and molecular sieving), Pd@ZIF-8 presents efficient, selective and recyclable catalytic hydrogenation of olefins. This is the first report of integrating the plasmonic photothermal effects of metal nanocrystals with MOFs to enhance catalytic activity.

MOF-derived nanomaterials

MOF-derived nanomaterials have been shown to be ideal sacrificial templates for fabricating various nanomaterials [307–317], including carbons, metal oxides, metal chalcogenides (metal sulfides and selenides), metal carbides, metal phosphides, and others. These nanomaterials have found wide applications in electrochemical energy storage and conversion as well as heterogeneous catalytic reactions including electrocatalysis,

organocatalysis, and photocatalysis. MOF-derived nanomaterials are usually made by thermolysis of the parent MOFs in the absence or presence of additional substances under an inert atmosphere, and some important advantages of the MOFs can be retained in the derived nanomaterials. The periodic structure of MOFs ensures that the active components are evenly dispersed in the nanomaterials. The high surface area of MOFs can also be inherited to a certain extent. Liu et al. firstly reported the thermal transformation of MOFs to porous carbon from MOF-5. The resultant porous carbon material exhibited high specific surface area and showed excellent electrochemical property as a supercapacitor [318]. The same group also obtained porous Co_3O_4 nanoparticles by the pyrolysis of Co-MOF in air. When served as an electrode material for LIB, the Co_3O_4 nanoparticles presented improved rate capability and prolonged cycle life [319]. By employing furfuryl alcohol and NH_4OH as the secondary carbon and nitrogen sources during the pyrolysis of ZIF-8, Aijaz et al. reported a high-surface-area N-decorated porous carbon which presented remarkable CO_2 adsorption capacities and CO_2/N_2 and CO_2/CH_4 selectivities [320]. Mostly importantly, the thermolysis treatment significantly improves the stability of parent MOF materials to give ultrastable nanostructures, which can withstand harsh conditions in reactions such as the Fischer-Tropsch process and the electrocatalyzed reactions. Through the pyrolysis of iron-containing MOFs, An et al. prepared a highly active iron-based catalyst for Fischer–Tropsch synthesis [321]. Lastly, MOF-derived carbon-based nanomaterials often possess greatly improved electrical conductivity than the parent MOFs. This is especially beneficial for electrocatalysis. For example, Pachfule et al. developed a self-templated, catalyst-free strategy to synthesize one-dimensional carbon nanorods which can be further transformed into two- to six-layered graphene nanoribbons through sonochemical treatment followed by chemical activation (Fig. 10e) [322]. The resulting graphene nanoribbons showed excellent supercapacitor performance. Despite the advantages, thermolysis still face challenges such as difficulty with controlling the reaction process as well as maintaining uniform structures for the whole nanomaterials and the active sites.

In recent years, MOF-derived nanomaterials containing single atoms or small atom clusters have received great attention. Yin et al. reported a strategy of achieving stable Co single atoms on nitrogen-doped porous carbon with over 4 wt% metal loading ratio [323]. A Zn/Co bimetallic MOF (BMOF) with homogeneous distribution of Zn and Co is synthesized by harvesting the same sodalite coordination behavior of both Co^{2+} and Zn^{2+} with 2-methylimidazole. The cobalt ions were reduced by carbonization of the organic linkers in BMOF and Zn is selectively evaporated away at a high temperature above 800 °C, leaving a nitrogen-doped porous carbon material containing evenly dispersed single Co atoms. The material exhibited superior ORR performance with a half-wave potential of 0.881 V. In a similar fashion, a series of nitrogen-doped porous carbon nanomaterials containing various single metal atoms were synthesized, in which the Fe nanomaterial was good for ORR [324], the Ru nanomaterial catalyzes the chemoselective hydrogenation of functionalized quinolones [325], the Ni nanomaterial catalyzes the electroreduction of CO_2 with a TOF of 5273 h^{-1} [224], and the Co nanomaterial with finely tuned coordinate nitrogen atoms catalyzes the electroreduction of CO_2 with even higher efficiency (TOF = 18,200 h^{-1}) [326]. Zhang et al. reported the preparation of atomic Fe catalyst from one-step thermal activation of Fe-doped ZIF frameworks [327]. The size of the catalyst particles can be tuned within 20 to 1000 nm by modifying the Fe-doped ZIF precursors. The optimized catalyst showed high ORR activity with $E_{1/2}$ of 0.85 V in 0.5 M H_2SO_4. Such MOF-derived nanomaterials contained earth-abundant metals and could potentially replace noble metal catalysts (like Pt) for ORR in acidic media. For such applications, Fe is not ideal since the presence of Fe and peroxide in electrodes generates free radicals capable of degrading the organic ionomer and the membrane, and the similar approach was adopted to make atomic Co catalyst for acidic ORR with $E_{1/2}$ of 0.80 V [328].

MOF precursors can also be used to generate nanomaterials containing ultrafine metal clusters. Wang et al. developed a host–guest strategy to construct an electrocatalyst with porphyrin-like Fe-Co dual sites embedded on nitrogen-doped porous carbon and demonstrated its activity for ORR in 0.1 M $HClO_4$ solution [329]. The catalyst had comparable performance to Pt/C with $E_{1/2}$ of 0.86 V. By incorporating $Ru_3(CO)_{12}$ during the synthesis of ZIF-8 followed by pyrolysis at 800 °C, Ji et al. prepared uniform Ru_3 clusters stabilized by nitrogen species in porous carbon [330]. This MOF-derived nanomaterial exhibited excellent catalytic activity (100% conversion), high chemoselectivity (100% for 2-aminobenzaldehyde), and much higher TOF (4320 h^{-1}) for oxidation of 2-aminobenzyl alcohol than Ru nanoparticles. So far there have only been limited reports on the MOF-derived nanomaterials containing single atoms or small atom clusters. Given the rich structural diversity of MOFs and the unique activities of single atom or atom clusters, we expect more synthetic strategies will be developed for these types of nanomaterials.

Quasi-MOFs

MOFs with high surface areas offer a great platform for various applications, but their inorganic nodes are partitioned by organic ligands and often show weak interactions with guests such as metal NPs. Recently, Tsumori et al. came up with a general approach for the preparation of "quasi-MOFs" which possess the transition-state-like structure between MOFs and metal oxides [331]. Via thermal transformation to partially remove the organic ligands, the obtained quasi-MOFs could expose the inorganic nodes to guests while largely retaining the porosity of the framework, resulting in enhanced interaction between MOFs and guests. Using Au NP/quasi-MIL-101 composite as an example, the researchers found that varying pyrolysis temperature could modulate the interface between Au NPs and Cr-O nodes in MIL-101 [331]. The optimized Au/quasi-MIL-101 shows high catalytic activity for CO oxidation at temperature down to 193 K, presenting a rare example of efficient catalyst for low-temperature CO oxidation.

Conclusions and outlook

Here, we have summarized the main structural characters and recent functional applications of MOFs. The MOF field has

undergone explosive growth especially in the past two decades, and the trend is continuing. While early applications of MOFs were focused on gas storage and separation due to their porous structures, more and more new applications such as catalysis, chemical sensors, proton conduction, and biomedicine are being developed. The structures of MOFs determine their functions, and the vast number of published MOF papers makes it possible to deduce structure–function relationships. For example, the gas storage and separation typically benefit from micropores, which match the sizes of particular gas molecules, while MOF composites and MOF catalysts often require meso- or macropores as well as open channels to facilitate mass transport. Compared to other traditional porous materials, MOFs have rich, highly ordered, and tunable structures. It is always fascinating to discover new MOF structures, but it suffices to say that the current emphasis of MOF research is on using structural information to either improve known functions or develop new functions of MOFs. MOFs can form composite materials with an endless list of other materials like metal nanoparticles, polymers, metal oxides, metal complexes, small organic molecules, and big biomolecules including enzymes and DNAs. The structures of MOFs can be finely tuned by direct or post-synthetic modification of the ligands, the metal SBUs, and inclusion of guest species.

Despite the significant progress in an ever-increasing list of MOF-related research areas, a number of challenges remain. First, the exact MOF growth mechanism remains obscure. A precise control of the target structures for pristine MOFs remains difficult due to the limited understanding of self-assembly in a closed reaction system, for instance, the effect of synthetic condition on increasing or decreasing the surface area and pore size of MOFs. Deep understanding of the self-assembly mechanism will allow us to design and construct suitable MOFs with regular or hierarchical pores, adjustable composition, and high surface area. Second, new strategies are still needed to construct MOF composite materials. It is always the goal of composite materials to synergistically combine the structural advantages of MOFs with the functions of the guest materials, but the experimental methods to achieve this are still limited. Third, the syntheses of many MOF-derived materials remain difficult to control. Despite the high surface area and high porosity of many MOF-derived materials, precise control on the shape and size of their pores is often missing. Lastly, from the perspective of practical applications, issues including cost, stability, electrical conductivity, etc., of MOFs for industrially important reactions still need to be addressed. Thus large-scale synthetic methods with high yield to afford low-cost MOFs are yet to be developed. Most practical applications of MOFs require high stability in the presence of moisture or water, but most MOFs have generally moderate to low stability in water. The stability of MOFs should be further improved under strongly acidic or basic conditions, despite the development of a number of MOFs with extremely high chemical and thermal stability. For electrocatalysis and related fields, most MOFs have shown poor electrical conductivity but many strategies have been developed to address the problem [332]. For applications such as MOF-based catalysis, most studies have been focused on proof of concepts. More important industrially relevant reactions such as oil cracking and refinery, polymerization, and asymmetric synthesis of various chiral intermediates for pharmaceuticals need to be explored.

In conclusion, MOFs have received tremendous advances from structural design and controllable synthesis to their functional applications in the past two decades. Although many obstacles remain to be solved on their way to the industrial applications, the academia and chemical industry are beginning to join hands to realize practical applications of MOFs. We expect a bright future for MOFs with the collaborative efforts from researchers in different fields including chemists, materials scientists, engineers, medical professionals, and others.

Acknowledgments

This work is supported by the NSFC (21725101, 21673213, 21871244 and 21521001), the 973 program (2014CB931803), the Fundamental Research Funds for the Central Universities (WK2060030029), and Troy University Faculty Development Fund.

References

[1] M. Hartmann et al., Chem. Soc. Rev. 45 (2016) 3313–3330.
[2] K. Kim et al., Nature 535 (2016) 131–135.
[3] B. Ruehle et al., J. Am. Chem. Soc. 139 (2017) 6663–6668.
[4] Y. Sun et al., Nat. Commun. 8 (2017) 252.
[5] B. Li et al., Adv. Mater. 28 (2016) 8819–8860.
[6] M.D. Allendorf, V. Stavila, CrystEngComm 17 (2015) 229–246.
[7] H. Furukawa et al., Science 341 (2013) 1230444.
[8] S. Qiu et al., Chem. Soc. Rev. 43 (2014) 6116–6140.
[9] J.-R. Li et al., Chem. Rev. 112 (2012) 869–932.
[10] L. Jiao et al., Adv. Mater. 30 (2017) 1703663.
[11] C.M. Doherty et al., Acc. Chem. Res. 47 (2014) 396–405.
[12] J.C. Tan, A.K. Cheetham, Chem. Soc. Rev. 40 (2011) 1059–1080.
[13] J.J. Perry IV et al., Chem. Soc. Rev. 38 (2009) 1400–1417.
[14] D.J. Tranchemontagne et al., Chem. Soc. Rev. 38 (2009) 1257–1283.
[15] W. Lu et al., Chem. Soc. Rev. 43 (2014) 5561–5593.
[16] V. Guillerm et al., Chem. Soc. Rev. 43 (2014) 6141–6172.
[17] H. Deng et al., Science 336 (2012) 1018–1023.
[18] K. Shen et al., Science 359 (2018) 206–210.
[19] N.C. Burtch et al., Chem. Rev. 114 (2014) 10575–10612.
[20] A.J. Howarth et al., Nat. Rev. Mater. 1 (2016) 15018.
[21] M. Bosch et al., Adv. Chem. 2014 (2014), https://doi.org/10.1155/2014/182327 182327.
[22] J. Duan et al., Coord. Chem. Rev. 332 (2017) 48–74.
[23] G. Férey et al., Science 309 (2005) 2040–2042.
[24] K.S. Park et al., Proc. Natl. Acad. Sci. 103 (2006) 10186–10191.
[25] X.-C. Huang et al., Angew. Chem. Int. Ed. 45 (2006) 1557–1559.
[26] J.H. Cavka et al., J. Am. Chem. Soc. 130 (2008) 13850–13851.
[27] H. Furukawa et al., J. Am. Chem. Soc. 136 (2014) 4369–4381.
[28] D. Feng et al., Angew. Chem. Int. Ed. 51 (2012) 10307–10310.
[29] W. Morris et al., Inorg. Chem. 51 (2012) 6443–6445.
[30] J.E. Mondloch et al., Chem. Commun. 50 (2014) 8944–8946.
[31] V. Bon et al., Cryst. Growth Des. 13 (2013) 1231–1237.
[32] H.-L. Jiang et al., J. Am. Chem. Soc. 134 (2012) 14690–14693.
[33] T. Loiseau et al., Chem. Eur. J. 10 (2004) 1373–1382.
[34] V. Colombo et al., Chem. Sci. 2 (2011) 1311–1319.
[35] J.G. Nguyen, S.M. Cohen, J. Am. Chem. Soc. 132 (2010) 4560–4561.
[36] C. Yang et al., J. Am. Chem. Soc. 133 (2011) 18094–18097.
[37] Z.-R. Jiang et al., NPG Asia Mat. 8 (2016) e253.
[38] S.J. Yang, C.R. Park, Adv. Mater. 24 (2012) 4010–4013.
[39] W. Zhang et al., J. Am. Chem. Soc. 136 (2014) 16978–16981.
[40] Y.-H. Shih et al., Chem. Eur. J. 23 (2017) 42–46.
[41] V. Singh et al., Chem. Commun. 53 (2017) 9246–9249.
[42] Y. Sun et al., J. Mater. Chem. A 5 (2017) 18770–18776.
[43] N. Ding et al., J. Am. Chem. Soc. 138 (2016) 10100–10103.
[44] X.-W. Zhu et al., Chem. Commun. 52 (2016) 6513–6516.
[45] R. Feng et al., Chem. Sci. 9 (2018) 950–955.
[46] J. Bae et al., Chem. Commun. 53 (2017) 12100–12103.

[47] R.G. Pearson, J. Am. Chem. Soc. 85 (1963) 3533–3539.
[48] Y. Bai et al., Chem. Soc. Rev. 45 (2016) 2327–2367.
[49] J. Duan et al., Adv. Funct. Mater. 23 (2013) 3525–3530.
[50] J. Duan et al., Chem. Sci. 5 (2014) 660–666.
[51] Y.-N. Gong et al., Chem. Sci. 7 (2016) 1070–1075.
[52] J. Dong et al., J. Am. Chem. Soc. 137 (2015) 15988–15991.
[53] X.-F. Lu et al., J. Am. Chem. Soc. 138 (2016) 8336–8339.
[54] J. Yang et al., Chem. Eur. J. 23 (2017) 631–636.
[55] F.-Y. Yi et al., Mater. Horiz. 2 (2015) 245–251.
[56] K. Wang et al., J. Am. Chem. Soc. 138 (2016) 914–919.
[57] X.-L. Lv et al., J. Am. Chem. Soc. 139 (2017) 211–217.
[58] I.A. Ibarra et al., Chem. Commun. 47 (2011) 8304–8306.
[59] D. Banerjee et al., Cryst. Growth Des. 9 (2009) 4922–4926.
[60] D. Banerjee et al., Cryst. Growth Des. 9 (2009) 2500–2503.
[61] K.W. Chapman et al., J. Am. Chem. Soc. 131 (2009) 17546–17547.
[62] S.M. Moosavi et al., ACS Cent. Sci. 4 (2018) 832–839.
[63] W. Xuan et al., Chem. Soc. Rev. 41 (2012) 1677–1695.
[64] G. Férey et al., Angew. Chem. Int. Ed. 43 (2004) 6296–6301.
[65] M. Eddaoudi et al., Science 295 (2002) 469–472.
[66] D. Bradshaw et al., Chem. Soc. Rev. 43 (2014) 5431–5443.
[67] W. Zhang et al., Adv. Mater. 27 (2015) 2923–2929.
[68] Y.-N. Wu et al., Angew. Chem. Int. Ed. 50 (2011) 12518–12522.
[69] H. Huang et al., Nat. Commun. 6 (2015) 8847.
[70] L.-G. Qiu et al., Angew. Chem. Int. Ed. 47 (2008) 9487–9491.
[71] M.-H. Pham et al., Cryst. Growth Des. 12 (2012) 1008–1013.
[72] K. Li et al., Angew. Chem. Int. Ed. 57 (2018) 3439–3443.
[73] S. Cao et al., Chem. Sci. 4 (2013) 3573–3577.
[74] G. Cai, H.-L. Jiang, Angew. Chem. Int. Ed. 56 (2017) 563–567.
[75] S. Yuan et al., Nat. Commun. 8 (2017) 15356.
[76] J.B. DeCoste et al., Chem. Eur. J. 21 (2015) 18029–18032.
[77] Y. Kim et al., Angew. Chem. Int. Ed. 54 (2015) 13273–13278.
[78] Y. Yue et al., J. Am. Chem. Soc. 135 (2013) 9572–9575.
[79] I. Senkovska, S. Kaskel, Chem. Commun. 50 (2014) 7089–7098.
[80] O.K. Farha et al., J. Am. Chem. Soc. 134 (2012) 15016–15021.
[81] N.L. Rosi et al., Science 300 (2003) 1127–1129.
[82] S.S. Kaye et al., J. Am. Chem. Soc. 129 (2007) 14176–14177.
[83] M.P. Suh et al., Chem. Rev. 112 (2012) 782–835.
[84] https://www.energy.gov/eere/fuelcells/hydrogen-storage.
[85] H. Furukawa et al., Science 329 (2010) 424–428.
[86] K. Sumida et al., J. Am. Chem. Soc. 131 (2009) 15120–15121.
[87] D. Lässig et al., Angew. Chem. Int. Ed. 50 (2011) 10344–10348.
[88] Y. He et al., Chem. Soc. Rev. 43 (2014) 5657–5678.
[89] T.A. Makal et al., Chem. Soc. Rev. 41 (2012) 7761–7779.
[90] J.A. Mason et al., Chem. Sci. 5 (2014) 32–51.
[91] Y. Peng et al., J. Am. Chem. Soc. 135 (2013) (1894) 11887–11891.
[92] J.-M. Lin et al., Angew. Chem. Int. Ed. 55 (2016) 4674–4678.
[93] J.A. Mason et al., Nature 527 (2015) 357–361.
[94] F. Gándara et al., J. Am. Chem. Soc. 136 (2014) 5271–5274.
[95] B. Li et al., J. Am. Chem. Soc. 136 (2014) 6207–6210.
[96] B. Li et al., Energy Environ. Sci. 8 (2015) 2504–2511.
[97] D. Alezi et al., J. Am. Chem. Soc. 137 (2015) 13308–13318.
[98] I. Spanopoulos et al., J. Am. Chem. Soc. 138 (2016) 1568–1574.
[99] Y. Liu et al., Greenh. Gases 2 (2012) 239–259.
[100] D. Britt et al., Proc. Natl. Acad. Sci. 106 (2009) 20637–20640.
[101] K. Sumida et al., Chem. Rev. 112 (2012) 724–781.
[102] J.-R. Li et al., Coord. Chem. Rev. 255 (2011) 1791–1823.
[103] S.R. Caskey et al., J. Am. Chem. Soc. 130 (2008) 10870–10871.
[104] A.M. Fracaroli et al., J. Am. Chem. Soc. 136 (2014) 8863–8866.
[105] T.M. McDonald et al., Nature 519 (2015) 303–308.
[106] P.-Q. Liao et al., Chem. Sci. 7 (2016) 6528–6533.
[107] P. Nugent et al., Nature 495 (2013) 80–84.
[108] K. Adil et al., Chem. Soc. Rev. 46 (2017) 3402–3430.
[109] Z.R. Herm et al., Chem. Mater. 26 (2014) 323–338.
[110] B. Li et al., J. Phys. Chem. Lett. 5 (2014) 3468–3479.
[111] H. Li et al., Mater. Today 21 (2018) 108–121.
[112] R.-B. Lin et al., Coord. Chem. Rev. (2017), https://doi.org/10.1016/j.ccr.2017.09.027.
[113] D. Banerjee et al., Acc. Chem. Res. 48 (2015) 211–219.
[114] Y. Peng et al., Science 346 (2014) 1356–1359.
[115] X. Cui et al., Science 353 (2016) 141–144.
[116] P.-Q. Liao et al., Science 356 (2017) 1193–1196.
[117] M. Fujita et al., J. Am. Chem. Soc. 116 (1994) 1151–1152.
[118] J. Lee et al., Chem. Soc. Rev. 38 (2009) 1450–1459.
[119] A. Corma et al., Chem. Rev. 110 (2010) 4606–4655.
[120] A.H. Chughtai et al., Chem. Soc. Rev. 44 (2015) 6804–6849.
[121] J. Gascon et al., ACS Catal. 4 (2014) 361–378.
[122] J. Liu et al., Chem. Soc. Rev. 43 (2014) 6011–6061.
[123] A. Dhakshinamoorthy et al., Chem. Soc. Rev. 44 (2015) 1922–1947.
[124] C.-D. Wu, M. Zhao, Adv. Mater. 29 (2017) 1605446.
[125] L. Zhu et al., Chem. Rev. 117 (2017) 8129–8176.
[126] S.M.J. Rogge et al., Chem. Soc. Rev. 46 (2017) 3134–3184.
[127] Y.-B. Huang et al., Chem. Soc. Rev. 46 (2017) 126–157.
[128] W. Tu et al., Adv. Mater. 30 (2018) 1707582.
[129] T. Zhang, W. Lin, Chem. Soc. Rev. 43 (2014) 5982–5993.
[130] S. Subudhi et al., Catal. Sci. Technol. 8 (2018) 679–696.
[131] H. Wang et al., Chem 2 (2017) 52–80.
[132] M. Wen et al., Chem. Asian J. 13 (2018) 1767–1779.
[133] J. Zhu et al., Coord. Chem. Rev. 359 (2018) 80–101.
[134] K. Schlichte et al., Microporous Mesoporous Mater. 73 (2004) 81–88.
[135] L. Alaerts et al., Chem. Eur. J. 12 (2006) 7353–7363.
[136] A. Henschel et al., Chem. Commun. (2008) 4192–4194.
[137] S. Horike et al., J. Am. Chem. Soc. 130 (2008) 5854–5855.
[138] Z. Li et al., J. Am. Chem. Soc. 138 (2016) 1977–1982.
[139] G. Akiyama et al., Adv. Mater. 23 (2011) 3294–3297.
[140] J.S. Seo et al., Nature 404 (2000) 982–986.
[141] J. Canivet et al., J. Am. Chem. Soc. 135 (2013) 4195–4198.
[142] T. Zhang et al., J. Am. Chem. Soc. 138 (2016) 3241–3249.
[143] B. Li et al., J. Am. Chem. Soc. 136 (2014) 1202–1205.
[144] Z. Li et al., J. Am. Chem. Soc. 140 (2018) 8082–8085.
[145] H.-L. Jiang et al., J. Am. Chem. Soc. 131 (2009) 11302–11303.
[146] H.-L. Jiang et al., J. Am. Chem. Soc. 133 (2011) 1304–1306.
[147] M. Zhao et al., Nature 539 (2016) 76–80.
[148] B. An et al., J. Am. Chem. Soc. 139 (2017) 3834–3840.
[149] Q. Yang et al., Nat. Commun. 8 (2017) 14429.
[150] G. Qiang et al., Angew. Chem. Int. Ed. 57 (2018) 4926–4930.
[151] G. Lu et al., Nat. Chem. 4 (2012) 310–316.
[152] S. Ahn et al., J. Am. Chem. Soc. 140 (2018) 8535–8543.
[153] G. Huang et al., Angew. Chem. Int. Ed. 55 (2016) 7379–7383.
[154] Y.-Z. Chen et al., J. Am. Chem. Soc. 139 (2017) 2035–2044.
[155] Y.-Z. Chen et al., ACS Catal. 5 (2015) 2062–2069.
[156] Q. Yang et al., Chem. Commun. 51 (2015) 10419–10422.
[157] M. Ding, H.-L. Jiang, ACS Catal. 8 (2018) 3194–3201.
[158] X. Sun et al., J. Catal. 357 (2018) 20–28.
[159] S. Wei et al., Nat. Nanotech. 13 (2018) 856–861.
[160] L. Ma et al., Chem. Soc. Rev. 38 (2009) 1248–1256.
[161] G. Nickerl et al., Chem. Ing. Tech. 83 (2011) 90–103.
[162] M. Yoon et al., Chem. Rev. 112 (2012) 1196–1231.
[163] C.-D. Wu et al., J. Am. Chem. Soc. 127 (2005) 8940–8941.
[164] M. Banerjee et al., J. Am. Chem. Soc. 131 (2009) 7524–7525.
[165] K. Mo et al., J. Am. Chem. Soc. 136 (2014) 1746–1749.
[166] Y. Liu et al., Angew. Chem. Int. Ed. 53 (2014) 13821–13825.
[167] Q. Han et al., Nat. Commun. 6 (2015) 10007.
[168] K. Meyer et al., Energy Environ. Sci. 8 (2015) 1923–1937.
[169] S. Wang, X. Wang, Small 11 (2015) 3097–3112.
[170] Y. Fang et al., Coord. Chem. Rev. 373 (2017) 83–115.
[171] J.-L. Wang et al., ACS Catal. 2 (2012) 2630–2640.
[172] A. Dhakshinamoorthy et al., Angew. Chem. Int. Ed. 55 (2016) 5414–5445.
[173] C. Xu et al., Chem. Sci. 9 (2018) 3152–3158.
[174] A. Fateeva et al., Angew. Chem. Int. Ed. 51 (2012) 7440–7444.
[175] J.-D. Xiao et al., Angew. Chem. Int. Ed. 57 (2018) 1103–1107.
[176] D. Li et al., Adv. Mater. 30 (2018) 1707377.
[177] H. Liu et al., Angew. Chem. Int. Ed. 57 (2018) 5379–5383.
[178] C.-C. Wang et al., Energy Environ. Sci. 7 (2014) 2831–2867.
[179] D. Shi et al., Chem. Sci. 6 (2015) 1035–1042.
[180] X.-L. Yang et al., J. Am. Chem. Soc. 134 (2012) 10638–10645.
[181] J. Long et al., Chem. Commun. 48 (2012) 11656–11658.
[182] L. Shen et al., J. Mater. Chem. A 1 (2013) 11473–11482.
[183] D. Sun et al., Appl. Catal., B 164 (2015) 428–432.
[184] M.A. Nasalevich et al., Chem. Commun. 49 (2013) 10575–10577.
[185] S. Abedi, A. Morsali, ACS Catal. 4 (2014) 1398–1403.
[186] P. Wu et al., J. Am. Chem. Soc. 134 (2012) 14991–14999.
[187] Y. Kataoka et al., Energy Environ. Sci. 2 (2009) 397–400.
[188] C.G. Silva et al., Chem. Eur. J. 16 (2010) 11133–11138.
[189] Z.-L. Wu et al., Angew. Chem. Int. Ed. 55 (2016) 4938–4942.
[190] C. Wang et al., J. Am. Chem. Soc. 134 (2012) 7211–7214.
[191] J.-D. Xiao et al., Angew. Chem. Int. Ed. 55 (2016) 9389–9393.

[192] T. Zhou et al., Energy Environ. Sci. 6 (2013) 3229–3234.
[193] S.-Y. Han et al., Angew. Chem. Int. Ed. 57 (2018) 9864–9869.
[194] H. Li et al., Angew. Chem. Int. Ed. 57 (2018) 3222–3227.
[195] X.-P. Wu et al., J. Am. Chem. Soc. 140 (2018) 7904–7912.
[196] T. Liao et al., J. Am. Chem. Soc. 140 (2018) 9159–9166.
[197] X. Fang et al., Adv. Mater. 30 (2018) 1705112.
[198] X. Zhao et al., Angew. Chem. Int. Ed. 57 (2018) 9790.
[199] J.-D. Xiao, H.-L. Jiang, Small 13 (2017) 1700632.
[200] C. Wang et al., J. Am. Chem. Soc. 133 (2011) 13445–13454.
[201] C. Wang et al., J. Am. Chem. Soc. 134 (2012) 19895–19908.
[202] B. Nepal, S. Das, Angew. Chem. Int. Ed. 52 (2013) 7224–7227.
[203] L. Chi et al., Small 12 (2016) 1351–1358.
[204] G. Paille et al., J. Am. Chem. Soc. 140 (2018) 3613–3618.
[205] Y. An et al., Angew. Chem. Int. Ed. 56 (2017) 3036–3040.
[206] Y. Fu et al., Angew. Chem. Int. Ed. 51 (2012) 3364–3367.
[207] H.-Q. Xu et al., J. Am. Chem. Soc. 137 (2015) 13440–13443.
[208] H. Zhang et al., Angew. Chem. Int. Ed. 55 (2016) 14310–14314.
[209] E.-X. Chen et al., Adv. Mater. 30 (2018) 1704388.
[210] T. Kajiwara et al., Angew. Chem. Int. Ed. 55 (2016) 2697–2700.
[211] Y. Wang et al., J. Am. Chem. Soc. 140 (2018) 38–41.
[212] P.-Q. Liao et al., Coord. Chem. Rev. 373 (2017) 22–48.
[213] J. Liu et al., ACS Catal. 8 (2018) 6707–6732.
[214] J. Liu et al., Adv. Energy Mater. 7 (2017) 1700518.
[215] S. Ma et al., Chem. Eur. J. 17 (2011) 2063–2067.
[216] Y.-Z. Chen et al., Adv. Mater. 27 (2015) 5010–5016.
[217] L. Shang et al., Adv. Mater. 28 (2016) 1668–1674.
[218] Q.-L. Zhu et al., Adv. Mater. 28 (2016) 6391–6398.
[219] L. Jiao et al., Angew. Chem. Int. Ed. 57 (2018) 8525–8529.
[220] L. Jiao et al., Chem. Sci. 7 (2016) 1690–1695.
[221] T.Y. Ma et al., J. Am. Chem. Soc. 136 (2014) 13925–13931.
[222] H.B. Wu et al., Nat. Commun. 6 (2015) 6512.
[223] G. Cai et al., Chem 2 (2017) 791–802.
[224] C. Zhao et al., J. Am. Chem. Soc. 139 (2017) 8078–8081.
[225] Y. Ye et al., Nano Energy 38 (2017) 281–289.
[226] F. Pan et al., ACS Catal. 8 (2018) 3116–3122.
[227] S. Mukherjee et al., Nano Energy 48 (2018) 217–226.
[228] W. Guo et al., Small Methods (2018) 1800204.
[229] Z. Geng et al., Adv. Mater. 30 (2018) 1803498.
[230] M. Jahan et al., J. Am. Chem. Soc. 134 (2012) 6707–6713.
[231] J.-Q. Shen et al., J. Am. Chem. Soc. 139 (2017) 1778–1781.
[232] S. Zhao et al., Nat. Energy 1 (2016) 16184.
[233] D. Zhu et al., Chem. Commun. 53 (2017) 10906–10909.
[234] J. Duan et al., Nat. Commun. 8 (2017) 15341.
[235] T. Wen et al., Mater. Horiz. (2018), https://doi.org/10.1039/C1038MH00859K.
[236] S. Mukhopadhyay et al., Angew. Chem. Int. Ed. 57 (2018) 1918–1923.
[237] X. Su et al., J. Am. Chem. Soc. 140 (2018) 11286–11292.
[238] J.-S. Qin et al., J. Am. Chem. Soc. 137 (2015) 7169–7177.
[239] Y.-P. Wu et al., Angew. Chem. Int. Ed. 56 (2017) 13001–13005.
[240] I. Hod et al., ACS Catal. 5 (2015) 6302–6309.
[241] N. Kornienko et al., J. Am. Chem. Soc. 137 (2015) 14129–14135.
[242] W.P. Lustig et al., Chem. Soc. Rev. 46 (2017) 3242–3285.
[243] B. Chen et al., Acc. Chem. Res. 43 (2010) 1115–1124.
[244] L.E. Kreno et al., Chem. Rev. 112 (2012) 1105–1125.
[245] Z. Hu et al., Chem. Soc. Rev. 43 (2014) 5815–5840.
[246] B. Yan, Acc. Chem. Res. 50 (2017) 2789–2798.
[247] F.-Y. Yi et al., ChemPlusChem 81 (2016) 675–690.
[248] S.S. Nagarkar et al., Angew. Chem. Int. Ed. 52 (2013) 2881–2885.
[249] H.-T. Zhang et al., Chem. Commun. 50 (2014) 12069–12072.
[250] H.-L. Jiang et al., J. Am. Chem. Soc. 135 (2013) 13934–13938.
[251] W.-W. Zhan et al., J. Am. Chem. Soc. 135 (2013) 1926–1933.
[252] B. Wang et al., J. Am. Chem. Soc. 138 (2016) 6204–6216.
[253] P. Ramaswamy et al., Chem. Soc. Rev. 43 (2014) 5913–5932.
[254] F. Yang et al., Nat. Energy 2 (2017) 877–883.
[255] S.S. Nagarkar et al., Angew. Chem. Int. Ed. 53 (2014) 2638–2642.
[256] F.-M. Zhang et al., J. Am. Chem. Soc. 139 (2017) 6183–6189.
[257] Y. Ye et al., J. Am. Chem. Soc. 139 (2017) 15604–15607.
[258] Y. Liu et al., Chem. Commun. 50 (2014) 10023–10026.
[259] D.J. Rocca et al., Acc. Chem. Res. 44 (2011) 957–968.
[260] P. Horcajada et al., Chem. Rev. 112 (2012) 1232–1268.
[261] M.-X. Wu, Y.-W. Yang, Adv. Mater. 29 (2017) 1606134.
[262] C. Doonan et al., Acc. Chem. Res. 50 (2017) 1423–1432.
[263] P. Horcajada et al., Angew. Chem. Int. Ed. 45 (2006) 5974–5978.
[264] J. An et al., J. Am. Chem. Soc. 131 (2009) 8376–8377.
[265] Q. Hu et al., J. Med. Chem. 57 (2014) 5679–5685.
[266] W.J. Rieter et al., J. Am. Chem. Soc. 130 (2008) 11584–11585.
[267] X. Meng et al., Sci. Adv. 2 (2016) e1600480.
[268] A. Helal et al., Natl. Sci. Rev. 4 (2017) 296–298.
[269] H. Deng et al., Science 327 (2010) 846–850.
[270] X. Kong et al., Science 341 (2013) 882–885.
[271] Y. Sun et al., Angew. Chem. Int. Ed. 55 (2016) 6471–6475.
[272] Z. Dong et al., J. Am. Chem. Soc. 139 (2017) 14209–14216.
[273] Z. Fang et al., Angew. Chem. Int. Ed. 54 (2015) 7234–7254.
[274] J. Ren et al., Coord. Chem. Rev. 349 (2017) 169–197.
[275] S. Dissegna et al., Adv. Mater. (2018) 1704501.
[276] H. Wu et al., J. Am. Chem. Soc. 135 (2013) 10525–10532.
[277] F. Vermoortele et al., J. Am. Chem. Soc. 135 (2013) 11465–11468.
[278] G.C. Shearer et al., Chem. Mater. 26 (2014) 4068–4071.
[279] C.A. Trickett et al., Angew. Chem. Int. Ed. 54 (2015) 11162–11167.
[280] M.R. DeStefano et al., Chem. Mater. 29 (2017) 1357–1361.
[281] Z.-R. Jiang et al., ChemSusChem 8 (2015) 878–885.
[282] M. Zhao et al., Small Methods 1 (2017) 1600030.
[283] P.-Z. Li et al., Chem. Commun. 47 (2011) 8436–8438.
[284] A. Gallego et al., Adv. Mater. 25 (2013) 2141–2146.
[285] Y. Peng et al., Angew. Chem. Int. Ed. 56 (2017) 9757–9761.
[286] T. Rodenas et al., Nat. Mater. 14 (2014) 48–55.
[287] M. Zhao et al., Adv. Mater. 27 (2015) 7372–7378.
[288] Y. Wang et al., Adv. Mater. 28 (2016) 4149–4155.
[289] Y. Huang et al., Adv. Mater. 29 (2017) 1700102.
[290] F. Cao et al., J. Am. Chem. Soc. 138 (2016) 6924–6927.
[291] L. Cao et al., J. Am. Chem. Soc. 139 (2017) 7020–7029.
[292] W. Shi et al., Angew. Chem. Int. Ed. 56 (2017) 9704–9709.
[293] L. Cao et al., Angew. Chem. Int. Ed. 55 (2016) 4962–4966.
[294] Y. Ding et al., J. Am. Chem. Soc. 139 (2017) 9136–9139.
[295] Q.-L. Zhu, Q. Xu, Chem. Soc. Rev. 43 (2014) 5468–5512.
[296] S. Li, F. Huo, Nanoscale 7 (2015) 7482–7501.
[297] T. Kitao et al., Chem. Soc. Rev. 46 (2017) 3108–3133.
[298] J. Juan-Alcaniz et al., J. Mater. Chem. 22 (2012) 10102–10118.
[299] H.R. Moon et al., Chem. Soc. Rev. 42 (2013) 1807–1824.
[300] Q. Yang et al., Chem. Soc. Rev. 46 (2017) 4774–4808.
[301] X. Lian et al., Chem. Soc. Rev. 46 (2017) 3386–3401.
[302] N. Yanai et al., Angew. Chem. Int. Ed. 47 (2008) 9883–9886.
[303] Z. Li et al., ACS Catal. 6 (2016) 5359–5365.
[304] A. Aijaz et al., J. Am. Chem. Soc. 134 (2012) 13926–13929.
[305] Q.-L. Zhu et al., J. Am. Chem. Soc. 135 (2013) 10210–10213.
[306] Q. Yang et al., Angew. Chem. Int. Ed. 55 (2016) 3685–3689.
[307] Y.V. Kaneti et al., Adv. Mater. 29 (2017) 1604898.
[308] S.-N. Zhao et al., Coord. Chem. Rev. 337 (2017) 80–96.
[309] K. Shen et al., ACS Catal. 6 (2016) 5887–5903.
[310] L. Oar-Arteta et al., Mater. Chem. Front. 1 (2017) 1709–1745.
[311] Y. Qian et al., Small 13 (2017) 1701143.
[312] W. Xia et al., Energy Environ. Sci. 8 (2015) 1837–1866.
[313] H.B. Wu, X.W. Lou, Sci. Adv. 3 (2017). eaap9252.
[314] K.J. Lee et al., Acc. Chem. Res. 50 (2017) 2684–2692.
[315] Z. Liang et al., Adv. Mater. 30 (2017) 1702891.
[316] Y.-Z. Chen et al., Coord. Chem. Rev. 362 (2018) 1–23.
[317] S. Dang et al., Nat. Rev. Mater. 3 (2017) 17075.
[318] B. Liu et al., J. Am. Chem. Soc. 130 (2008) 5390–5391.
[319] B. Liu et al., J. Power Sources 195 (2010) 857–861.
[320] A. Aijaz et al., J. Am. Chem. Soc. 136 (2014) 6790–6793.
[321] B. An et al., ACS Catal. 6 (2016) 3610–3618.
[322] P. Pachfule et al., Nat. Chem. 8 (2016) 718–724.
[323] P. Yin et al., Angew. Chem. Int. Ed. 55 (2016) 10800–10805.
[324] Y. Chen et al., Angew. Chem. Int. Ed. 56 (2017) 6937–6941.
[325] X. Wang et al., J. Am. Chem. Soc. 139 (2017) 9419–9422.
[326] X. Wang et al., Angew. Chem. Int. Ed. 57 (2018) 1944–1948.
[327] H. Zhang et al., J. Am. Chem. Soc. 139 (2017) 14143–14149.
[328] X.X. Wang et al., Adv. Mater. 30 (2018) 1706758.
[329] J. Wang et al., J. Am. Chem. Soc. 139 (2017) 17281–17284.
[330] S. Ji et al., J. Am. Chem. Soc. 139 (2017) 9795–9798.
[331] N. Tsumori et al., Chem 4 (2018) 845–856.
[332] L. Sun et al., Angew. Chem. Int. Ed. 55 (2016) 3566–3579.